Nonlinear Climate Responses to Increasing CO_2 and Anthropogenic Aerosols Simulated by CESM1

Jiechun Deng[1,2*], Aiguo Dai[2] and Haiming Xu[1]

1 Key Laboratory of Meteorological Disaster, Ministry of Education (KLME)/Joint International Research Laboratory of Climate and Environmental Change (ILCEC)/ Collaborative Innovation Center on Forecast and Evaluation of Meteorological Disasters (CIC-FEMD), Nanjing University of Information Science and Technology, Nanjing 210044, China

2 Department of Atmospheric and Environmental Sciences, University at Albany, State University of New York, Albany, NY 12222, USA

Submitted to *J. Climate*

Submission Date: March 9, 2019

1st Revision Date: August 7, 2019

2nd Revision Date: September 24, 2019

*Corresponding author:

Jiechun Deng

School of Atmospheric Sciences, Nanjing University of Information Science and Technology, Nanjing 210044, China; E-mail: jcdeng@nuist.edu.cn

Early Online Release: This preliminary version has been accepted for publication in *Journal of Climate*, may be fully cited, and has been assigned DOI 10.1175/JCLI-D-19-0195.1. The final typeset copyedited article will replace the EOR at the above DOI when it is published.

Abstract

Atmospheric CO_2 and anthropogenic aerosols (AA) have increased simultaneously. Because of their opposite radiative effects, these increases may offset each other, which may lead to some nonlinear effects. Here the seasonal and regional characteristics of this nonlinear effect from the CO_2 and AA forcing are investigated using the fully coupled Community Earth System Model. Results show that nonlinear effects are small in the global-mean of the top-of-atmosphere radiative fluxes, surface air temperature and precipitation. However, significant nonlinear effects exist over the Arctic and other extratropical regions during certain seasons. When both forcings are included, Arctic sea ice in September-October-November decreases less than the linear combination of the responses to the individual forcings due to a higher sea-ice sensitivity to the CO_2-induced warming than the sensitivity to the AA-induced cooling. This leads to less Arctic warming in the combined-forcing experiment due to reduced energy release from the Arctic Ocean to the atmosphere. Some nonlinear effects on precipitation in June-July-August are found over East Asia, with the northward shifted East Asian summer rain belt to oppose the CO_2 effect. In December-January-February, the aerosol loading over Europe in the combined-forcing experiment is higher than that due to the AA forcing, resulting from CO_2-induced circulation changes. The changed aerosol loading results in regional thermal responses due to aerosol direct and indirect effects, weakening the combined changes of temperature and circulation. This study highlights the need to consider nonlinear effects from historical CO_2 and AA forcing in seasonal and regional climate attribution analyses.

Accepted for publication in *Journal of Climate*. DOI 10.1175/JCLI-D-19-0195.1.

1. Introduction

Emissions of greenhouse gases (GHGs) and anthropogenic aerosols (AA), two major anthropogenic forcings, have been increasing simultaneously over the last century due to fossil fuel burning, deforestation, and other human activities. The GHG-induced radiative forcing for the period of 1750–2011 was estimated to be around 2.83 ± 0.57 $W \cdot m^{-2}$, while the concurring AA-induced forcing was around -1.0 ± 0.9 $W \cdot m^{-2}$ (Myhre et al. 2013). This reflects their well-known opposite thermal effects on the climate system.

The individual effects of GHGs and AA on the climate system have been widely investigated using single-forcing simulations, including their effects on Asian monsoon systems (e.g., Menon et al. 2002; Li et al. 2010; Sun et al. 2010; Ganguly et al. 2012; Wu et al. 2013; Deng and Xu 2016; Chen et al. 2018) and tropical circulation and rainfall (e.g., Clement et al. 1996; Held and Soden 2006; Kim et al. 2006; Collins et al. 2010; Ming et al. 2011; Lewinscahla et al. 2013). Aerosol direct radiative forcing can strengthen the South Asian Summer Monsoon (SASM) via the "elevated heat pump" (Lau et al. 2006); in contrast, the GHG-induced global warming would weaken the SASM circulation due to reduced upper-tropospheric land-sea thermal contrast (Sun et al. 2010; Dai et al. 2013) and the meridional temperature gradient (Sooraj et al. 2015). In the tropics, the time-mean vertical motion in the tropics is generally weakened by the GHG-induced global warming, in which the Walker circulation is more suppressed than the Hadley circulation (Vecchi and Soden 2007) due to uniform sea surface temperature (SST) warming and larger land surface warming (Zhang and Li 2017). Unlike well-mixed GHGs, the AA-induced cooling tends to strengthen the tropical circulation, but the asymmetric cooling due to the geographical distribution of aerosols acts to

Accepted for publication in *Journal of Climate*. DOI10.1175/JCLI-D-19-0195.1.

enhance the Hadley cell over the Southern Hemisphere (SH) while to weaken it over the Northern Hemisphere (NH; Ming and Ramaswamy 2011). The interhemispheric asymmetric cooling induced by AA (Rotstayn and Lohmann 2002) can further lead to a southward shift of the Intertropical Convergence Zone (ITCZ; William et al. 2001; Ming and Ramaswamy 2009; Wang et al. 2013; Allen et al. 2015). These findings indicate that the GHG and AA forcing can produce competing climate responses when applied separately in a model, and these compensating effects may partially offset each other when the forcings are applied together, potentially leading to some nonlinear effects.

Many historical climate change simulations (Taylor et al. 2012) have also applied the time-varying GHG and AA forcing separately with the goal to quantify their individual contributions to observed historical warming and other climate changes, with the implicit assumption that the responses to these forcings are linearly additive with negligible nonlinear effects when they are applied together (e.g., Song et al. 2014; Kjellsson 2015; Gagné et al. 2017; Lau and Kim 2017). Similar SST response patterns (but with opposite signs) to the GHG and AA forcing are found despite that the aerosol emissions and loadings are geographically concentrated (Xie et al. 2013). This suggests that SST and other climate responses may be independent of the spatial patterns of radiative forcing. Comparisons between the single- and all-forcing simulations show that the GHG effect dominates the rainfall trend over the oceanic monsoon region (Zhang and Li 2016), while aerosol forcing dominates over East Asia, causing a general drying trend over East Asia in the all-forcing simulations (Li et al. 2015) and a decadal weakening in low-level East Asian summer monsoon (EASM) circulation (Song et al. 2014). Tian et al. (2018) further pointed out that both GHGs and AA are anthropogenic drivers of recent changes in East Asian summer

Accepted for publication in *Journal of Climate*. DOI10.1175/JCLI-D-19-0195.1.

rainfall since the mid-1990s but with different contributions. In addition, when both forcing agents are considered, aerosol forcing dominates the interhemispheric asymmetric climate response in historical all-forcing simulations (Wang et al. 2016a), and the simulated southward cross-equatorial surface winds and equatorial precipitation over the past 60 years resemble those of aerosol forcing rather than GHG forcing, as well as those from observations (Wang et al. 2016b).

Clearly, the validity of some of these conclusions depends on whether the nonlinear effect from the interactions of the different forcing agents, which occur simultaneously in reality, is indeed small and thus can be ignored, as suggested previously (e.g., Song et al. 2014; Gagné et al. 2017; Lau and Kim 2017). One potential nonlinear effect could result from the combination of the GHG and AA forcing, which may cause some nonlinear responses due to their opposite radiative effects. Thus, it is possible that the combined effect of the GHG and AA forcing may differ from the combination of their individual effects by the GHG or AA forcing alone. To our knowledge, this issue has not been systematically investigated, although there have been some attempts to evaluate the nonlinear aspect of the combined GHG and AA effects. For example, Feichter et al. (2004) found that the global warming is smaller than the linear combination of individual changes when combing GHG and aerosol forcing together; Ming and Ramaswamy (2009) suggested that aerosol-induced surface cooling could be amplified at high latitudes via surface albedo feedback when GHG and aerosol changes are simultaneously included in a climate model, implying nonlinearity in Arctic climate response, and their further investigation (Ming et al. 2011) links the cause of the nonlinearity to tropopause height changes. However, these studies focused on the annual- and zonal-mean climate responses due to the nonlinear

Accepted for publication in *Journal of Climate*. DOI10.1175/JCLI-D-19-0195.1.

effect.

This study aims to address following questions by performing and analyzing a series of numerical experiments using prescribed CO_2 and AA forcing: 1) when and where would nonlinear climate responses to CO_2 and AA forcing arise in temperature, precipitation, and large-scale atmospheric circulation? 2) what are the roles of these nonlinear changes in shaping the climate responses to the two forcing agents? and 3) what are the possible mechanisms leading to the nonlinear effects? This study differs from previous similar studies (Feichter et al. 2004; Ming and Ramaswamy 2009; Ming et al. 2011; Song et al. 2014; Wang et al. 2016a; Zhang and Li 2016; Lau and Kim 2017) in that the seasonal and regional characteristics of the nonlinear response and the underlying physical processes are examined. Our new findings include that 1) the nonlinear effect on the climate occurs over certain regions during some seasons and 2) the asymmetry in Arctic sea-ice response to CO_2-induced warming and AA-induced cooling and the changed aerosol loading play major roles in causing the nonlinear climate responses.

The remainder of the paper is organized as follows. In section 2, we describe the methodology, including the model, experimental design and signal detection. Section 3 examines seasonal climate responses to single and combined forcing globally and regionally, with a specific focus on the nonlinear aspects. The possible mechanisms for the nonlinear climate response are also explored in section 3. Conclusions and discussions are provided in section 4.

2. Methodology

Accepted for publication in *Journal of Climate*. DOI10.1175/JCLI-D-19-0195.1.

a. Model and experiments

We used a fully-coupled climate model, namely, the version 1.0.3 of the Community Earth System Model (CESM1) released by the National Center for Atmospheric Research (Hurrell et al. 2013). The CESM1 includes four interacting components: the Community Atmosphere Model version 5 (CAM5.1; Neale et al. 2012), the Community Land Model version 4 (CLM4), the Parallel Ocean Program (POP2), and the Community Ice CodE version 4 (CICE4). The atmosphere component used in this study has a horizontal grid spacing of 1.9° latitude × 2.5° longitude and a hybrid vertical coordinate with 30 levels. The ocean and sea-ice components have a horizontal grid spacing of approximate 1° on a tri-polar coordination.

To explore nonlinear effects on the global and regional climate due to increasing CO_2 and AA, four numerical experiments are conducted (Table 1). The control experiment (CTL) was run with the B1850C5 component setting provided by the model; that is, the values of all external forcing agents were prescribed at levels for year 1850, including CO_2 and aerosols. The other experiments are the same as CTL, except using only CO_2 forcing (GHG), only AA forcing (AER), and both CO_2 and AA forcing (BOTH) globally at the level for year 2000. The atmospheric CO_2 content was prescribed at 284.7 and 367 ppmv, respectively, for year 1850 and 2000. Anthropogenic aerosol emissions for year 1850 and 2000 (Fig. 1) were those used in IPCC AR5 (Lamarque et al. 2010), including black carbon, organic carbon, and sulfur aerosol emissions. Figure 1 clearly shows that West Europe and North America were two major emission sources in 1850, while in 2000 East and South Asian emissions increased sharply and dominated global aerosol sources. All experiments were integrated for 200 model years from a state obtained from a pre-industrial control run. The output of the last 150 years from all

Accepted for publication in *Journal of Climate*. DOI10.1175/JCLI-D-19-0195.1.

experiments were analyzed and often averaged (to smooth out internal variations) when the simulated climate generally reached a new steady state, although the CO_2 forcing appears to continue to cause some warming in the GHG and BOTH experiments (Fig. 2). This should not affect our results on the nonlinear effect, especially if one is interested in the transient response, which is the case for the real world. Since the 200 years of simulation contain different realizations of the internal variability with identical external forcing in each year, the averaging over the last 150 years for each experiment greatly reduces internal variations (to about $1/\sqrt{150}$ = 8% of those in individual years) in averaged fields, thus substantially enhancing the signal (= forced response) to noise (= internal variations) ratio.

b. Detection of nonlinear effects

To analyze the temporal and spatial characteristics of the nonlinear climate responses, the nonlinear change of a given variable is first obtained using the above experiments. The differences between GHG and CTL, AER and CTL, and BOTH and CTL can be considered as the climate responses to single CO_2 forcing (CO_2 effect), single AA forcing (aerosol effect), and their combined forcing (combined effect), respectively (Table 1). When both CO_2 and AA forcing are considered, their interaction may produce an effect that differs from the linear combination of the single-forcing effects. Thus, we quantify the nonlinear effect on a given variable as follows: *Nonlinear effect = Combined effect – CO_2 effect – Aerosol effect*. Thus, the nonlinear effect can be regarded as the residual between the combined effect from the BOTH experiment and the linear combination of individual effects from the GHG and AER experiments.

Accepted for publication in *Journal of Climate*. DOI10.1175/JCLI-D-19-0195.1.

c. Inferred and potential responses of Arctic sea ice

When both CO_2 and AA forcing are included in the model, their nonlinear effect yields significantly less Arctic sea-ice loss in September-October-November (SON) than the linear combination of the CO_2 and AA alone experiments (see section 3a). To better understand the processes leading to this nonlinear effect on sea ice concentration (SIC), we analyzed Arctic SIC changes due to the individual effects. We first calculated the Arctic SIC sensitivity (Γ) to CO_2-induced warming or AA-induced cooling as follows in the individual forcing runs:

$$\Gamma_{GHG} = \Delta SIC_{GHG}/|\Delta Tas_{GHG}|, \tag{1}$$

$$\Gamma_{AER} = \Delta SIC_{AER}/|\Delta Tas_{AER}|, \tag{2}$$

where the subscript denotes the forcing experiments, Δ(·) indicates the mean changes relative to the CTL experiment averaged over the Arctic region (70°–90°N), and Tas is surface air temperature. Thus, Γ_{GHG} (Γ_{AER}) means the decreased (increased) SIC per 1℃ Arctic warming (cooling), and Γ_{GHG} is negative while Γ_{AER} is positive. Please note that the SIC response would provide a positive feedback to enlarge the original Tas change (Dai et al. 2019), which is included in this definition. Accordingly, the linear SIC change from the two forcings can be written as:

$$\Delta SIC_{Linear} = \Delta Tas_{GHG} \times \Gamma_{GHG} - \Delta Tas_{AER} \times \Gamma_{AER}. \tag{3}$$

In BOTH experiment, the Arctic Tas change is close, but not equal (due to the nonlinear effect), to the linear combination of the Tas changes from the single forcing experiments with net warming over the Arctic (see Fig. 7), that is, $\Delta Tas_{BOTH} \approx \Delta Tas_{GHG} + \Delta Tas_{AER}$ and it is positive. Thus, the SIC changes in the BOTH experiment should be inferred using the SIC

Accepted for publication in *Journal of Climate*. DOI10.1175/JCLI-D-19-0195.1.

sensitivity to Arctic warming (i.e., Γ_{GHG}) as for the GHG experiment. Thus, the SIC changes in the BOTH experiment may be estimated as:

$$\Delta SIC_{BOTH,inferred} = (\Delta Tas_{GHG} + \Delta Tas_{AER}) \times \Gamma_{GHG}. \quad (4)$$

As a result, the nonlinear SIC changes can also be inferred by subtracting eq. (3) from eq. (4):

$$\Delta SIC_{Nonlienar,inferred} = \Delta Tas_{AER} \times (\Gamma_{GHG} + \Gamma_{AER}). \quad (5)$$

In eq. (5), the term ΔTas_{AER} is always negative (Fig. 7c), so the term $(\Gamma_{GHG} + \Gamma_{AER})$ determines the sign of inferred changes of the Arctic SIC. Later we will show that due to asymmetric SIC responses to ΔTas_{GHG} and ΔTas_{AER} (i.e., $\Gamma_{AER} < -\Gamma_{GHG}$), the inferred nonlinear effect from eq. (5) is generally positive from June to November. This helps us understand the nonlinear effect on SIC in the BOTH experiment.

Note that in deriving eqs. (4-5), we only assumed that the Tas change in the BOTH experiment is close to the linear combination of the Tas changes from the individual forcing simulations, as shown by Fig. 7 below. This allows us to diagnose and reveal the primary causes of the nonlinear SIC change. As shown below (Fig. 7), the inferred changes based on eqs. (4-5) are comparable to those computed directly from the BOTH experiment, which suggests that the above analysis is reasonable.

To explain the asymmetric responses of SIC to ΔTas in the GHG and AER experiments, we use the forced ΔTas and the CTL Tas to further calculate the percentage of the Arctic areas where sea ice was expected to melt or grow as the Tas deviates from the freezing point in response to the CO_2 or AA forcing, and we call this as the potential SIC change. For example, in the GHG experiment, the potential sea-ice loss can be described by the percentage of Arctic areas where CTL Tas is in a threshold interval of $(-\Delta Tas_{GHG}, 0)$ as follows:

Accepted for publication in *Journal of Climate*. DOI10.1175/JCLI-D-19-0195.1.

$$\Delta SIC_{GHG,potential} = -\frac{N_{-\Delta Tas_{GHG}<Tas_{CTL}<0}}{N_{Arctic}} \times 100\%, \quad (6)$$

where N_{Arctic} is the number of model grid boxes over the Arctic Ocean (70°–90°N), and $N_{-\Delta Tas_{GHG}<Tas_{CTL}<0}$ is the number of Arctic ocean grid boxes whose CTL Tas (in ℃) is within the $(-\Delta Tas_{GHG}, 0)$ range. Thus, the CO_2-induced warming would potentially melt the sea ice in these areas. Note here we ignored the difference of the freezing point between sea water (about -1.8℃) and freshwater (0℃), as Arctic sea ice ejects most of the salt in original sea water. Similarly, potential sea-ice growth under AA-induced cooling can be estimated as:

$$\Delta SIC_{AER,potential} = \frac{N_{0<Tas_{CTL}<-\Delta Tas_{AER}}}{N_{Arctic}} \times 100\%. \quad (7)$$

As shown later, there are larger Arctic areas where the mean Tas in CTL is just a few degrees Celsius below the freezing point than the areas a few degrees Celsius above the freezing point in the boreal early autumn, resulting in higher SIC sensitivity to the CO_2-induced warming than that to the AA-induced cooling (i.e., $\Gamma_{AER} < -\Gamma_{GHG}$). These analyses allow us to diagnose the causes of the asymmetric SIC responses to the CO_2-induced warming and AA-induced cooling, and their roles in producing the nonlinear SIC change when both forcing agents are included.

d. Moisture budget diagnosis

To quantify and understand the thermodynamic and dynamic contributions to the rainfall changes induced by anthropogenic forcing, the atmospheric moisture budget analysis is applied following Li et al. (2015). The total change in the mean moisture convergence (δMC) can be separated into two terms: the thermodynamic (δTH) and dynamic (δDY) components, which can be expressed as follows:

Accepted for publication in *Journal of Climate*. DOI10.1175/JCLI-D-19-0195.1.

$$\delta\overline{MC} \approx -\frac{1}{g\rho_w}\nabla\cdot\sum_{k=1}^{K}\overline{\boldsymbol{u}}_{k,c}\delta\bar{q}_k\overline{\Delta p}_k + \left(-\frac{1}{g\rho_w}\nabla\cdot\sum_{k=1}^{K}\delta\overline{\boldsymbol{u}}_k\bar{q}_{k,c}\overline{\Delta p}_k\right)$$

$$= \delta\overline{TH} + \delta\overline{DY}\ , \tag{8}$$

where g represents the gravity, ρ_w is the density of water, $\boldsymbol{u}$ is the horizontal wind vectors, q is specific humidity, and p is pressure. Here k is the index for vertical levels from 1000 to 200 hPa, and Δp is the layer pressure thickness. $(\cdot)_c$ and $\delta(\cdot)$ indicate the value from the control experiment and the differences between the forced and control experiments, respectively. All the meteorological variables used here are monthly values, and the overbar denotes the 150-year climatological mean.

3. Results

a. Response of surface air temperature and the role of Arctic sea ice

Figure 2a shows that the global-mean net radiation at the top of atmosphere (TOA) in the GHG (AER) experiment is generally larger (smaller) than that in the CTL experiment. For our setup, the CO_2-induced positive radiative forcing (relative to CTL) at TOA is comparable in magnitude to the AA-induced negative radiative forcing (Fig. 3a), although the CO_2 forcing experiment took longer than the AA forcing experiment to reach a steady state (Fig. 2). Thus, they are roughly canceled with each other in the BOTH experiment (Figs. 2a, 3a). However, the AA forcing induces much stronger net longwave (LW) and shortwave (SW) fluxes at TOA in magnitude than the CO_2 forcing (Figs. 3b-c). As seen in Table 2, the all-sky net SW flux at TOA increases by 0.82 $W\cdot m^{-2}$ due to the CO_2 forcing, while it declines by 2.76 $W\cdot m^{-2}$ due to the AA forcing. The direct effects of the CO_2 and AA forcing (i.e., the clear-sky net SW) are roughly canceled with each other in the BOTH experiment. However, the indirect effect of the

Accepted for publication in *Journal of Climate*. DOI10.1175/JCLI-D-19-0195.1.

AA forcing (Towmey 1974; Albrecht 1989) induces much larger net SW changes at TOA (i.e., the cloudy-sky net SW) via increased clouds. As a result, the AA-induced negative LW and SW forcing dominates (but offsets each other) in the BOTH experiment. Furthermore, the TOA radiative fluxes from the BOTH experiment are very close to the linear combination from the GHG and AER experiments, indicating small nonlinear effects for the TOA fluxes.

Global-mean responses of surface air temperature (Tas) generally agree well with the TOA radiative forcing except that the CO_2 forcing produces slightly larger warming to outweigh the aerosol cooling effect, resulting in a small net warming in the combined experiment (Fig. 2b). Again, the linear combination of the Tas responses matches the Tas response from the BOTH experiment, indicating small nonlinear effect in global-mean Tas changes. The nonlinear effect is also small for global-mean precipitation (Fig. 2c), although its response to the AA forcing substantially exceeds that to the CO_2 forcing, despite their comparable radiative and Tas responses. As a result, global-mean precipitation in the BOTH experiment decreases noticeably from the CTL experiment. This issue is examined further below.

The world-wide surface warming (cooling) induced by the CO_2 (AA) forcing is found in all seasons, although with considerable spatial variations (Fig. 4). The CO_2 forcing warms the lands more strongly than the oceans at mid-high latitudes over the NH (Figs. 4a-d), because of the relatively low evaporation rate and heat capacity of land (Sutton et al. 2007). However, the Arctic warming is much stronger and faster than the rest of the world, a phenomenon known as the Arctic amplification (e.g., Holland and Bitz 2003; Screen and Simmonds 2010; Barnes and Polvani 2015). This amplified Arctic warming is most evident in the cold season (Figs. 4a, d) due to the large surface heating from newly exposed waters during the cold season (Dai et al.

Accepted for publication in *Journal of Climate*. DOI10.1175/JCLI-D-19-0195.1.

2019). Similar spatial patterns also occur for the aerosol effect but with an opposite sign, including the enhanced cooling over the Arctic and land (Figs. 4e-h). Furthermore, aerosol source regions like East and South Asia see larger local surface cooling. We also notice the significant cooling over the North Pacific induced by the AA, which is advected to downwind regions from the sources by atmospheric winds (Fig. 1c; Yeh et al. 2013; Boo et al. 2015).

However, when both forcing factors are included in the model, the AA-induced surface cooling dominates the middle latitudes over the NH, especially over the oceans and the AA source regions, whereas large surface warming is seen mainly in the polar regions (Figs. 4i-l). The Tas change patterns from the BOTH experiment is highly correlated (r=0.82–0.91; Figs. 4i-l) with those from a linear combination of the Tas changes from the GHG and AER experiments, although they differ in magnitude. This similarity results in small nonlinear effects on Tas over most of the globe in all seasons (Fig. 5). Nevertheless, significant nonlinear Tas response is found over central-northern Europe and the Hudson Bay in December-January-February (DJF; Fig. 5a), around Antarctica in June-July-August (JJA; Fig. 5c), and over the Arctic Ocean in September-October-November (SON; Fig. 5d).

In the following, we focus on the Arctic cooling from the nonlinear effect in SON, as the European Tas response in DJF will be discussed in section 3c. The CESM1 can realistically simulate the spatial variations and mean seasonal cycle of Arctic SIC and has been applied to study the impact of sea-ice loss in many studies (see Dai et al. 2019 and refs therein). The Arctic SIC from our BOTH experiment is also found to capture the spatial and seasonal variations seen in the ERA-Interim reanalysis (Dee et al. 2011) (not shown). The SON nonlinear Arctic cooling is largest over the Pacific side, and is accompanied by the warming around the coastal

Accepted for publication in *Journal of Climate*. DOI10.1175/JCLI-D-19-0195.1.

regions surrounding the Barents Sea and the Kara Sea (Fig. 6a). This Tas nonlinear response pattern is highly anti-correlated (r=-0.9) with the SIC nonlinear response pattern (Fig. 6b) over the Arctic (north of 65°N), suggesting a connection between the two. As shown by Dai et al. (2019), the positive (negative) SIC response in SON (Fig. 6b) should reduce (increase) the open water surfaces and therefore decrease (increase) oceanic heating of the lower troposphere through decreased (increased) upward longwave (LW) radiation (Fig. 6c) and turbulent heat fluxes (Fig. 6d), as the Arctic Ocean is a heat source of the cold air in SON (Dai et al. 2019). The reduced (increased) oceanic heating would lead to colder (warmer) Tas, which in turn would increase (decrease) sea-ice cover, leading to a positive feedback loop. This mechanism by which Arctic sea-ice changes can affect Tas is consistent with previous studies (Deser et al. 2010; Screen and Simmonds 2010; Dai et al. 2019). Note that the Arctic cooling is strongly related to the reduced upward LW radiation, while the enhanced turbulent heat fluxes play a bigger role for the coastal warming around the Arctic where SIC decreases in the nonlinear effects (Fig. 6).

The above analysis does not, however, explain what triggers this positive feedback loop between Tas and SIC that would eventually lead to the nonlinear effects shown in Fig. 6. The seasonal sea-ice melting from May to September (Fig. 7a) allows the exposed Arctic water to absorb solar radiation in the warm season (Dai et al. 2019). The absorbed energy is then largely released to heat the atmosphere in the cold season from October to April via LW radiation and turbulent heat fluxes (Serreze and Barry 2011; Dai et al. 2019). The CO_2-induced global warming decreases the SIC throughout the year but mainly from June-December, and the warming amplification occurs mainly from October-December (Fig. 7b). It is roughly the

Accepted for publication in *Journal of Climate*. DOI10.1175/JCLI-D-19-0195.1.

opposite for the AA-induced cooling case with smaller changes (Fig. 7c). As a result, their linear combination (Fig. 7d) shows some SIC reduction and noticeable Arctic warming, especially for October-January. In contrast, the SIC reduction and Arctic warming from October-January are considerably smaller in the BOTH experiment (Fig. 7e) than the linear combination (Fig. 7d), which results in significant nonlinear effects for SIC from July-December and Tas mainly from October-November (Fig. 7f).

Figures 7b-c show that Γ_{GHG} is larger than Γ_{AER} in magnitude from July-November, suggesting that a 1℃ warming would cause a larger amount of sea-ice loss than the amount of sea-ice growth caused by a 1℃ cooling. As a result, the term $(\Gamma_{GHG} + \Gamma_{AER})$ in eq. (5) is negative from June to November (Fig. 7d), which would result in a positive nonlinear response for Arctic sea ice (blue bars in Fig. 7f). Physically, the reduced sea-ice loss in BOTH results from the reduced net Arctic warming in BOTH, as the AA forcing partially cancels some of the warming induced by the CO_2 forcing; while this warming causes more sea-ice loss in the GHG experiment than the sea-ice gain caused by the same amount of cooling in the AER experiment due to the asymmetric SIC sensitivities. The inferred SIC responses (blue bars in Figs. 7e-f) derived by only using changes of SIC and Tas in the GHG and AER experiments are highly correlated with those simulated by the BOTH experiment (gray bars in Fig. 7e-f), with some differences in magnitude due to some nonlinear effects from the SIC-Tas feedback in the BOTH experiment. These results suggest that the asymmetric SIC sensitivities to the CO_2-induced warming and AA-induced cooling can largely explain the nonlinear SIC response seen in the BOTH experiment.

Why would the Arctic SIC exhibit asymmetric sensitivities to the warming and cooling?

Accepted for publication in *Journal of Climate*. DOI10.1175/JCLI-D-19-0195.1.

According to eqs. (6) and (7), there are larger Arctic areas where the mean Tas in CTL is just a few degrees Celsius below the freezing point than the areas where the Tas in CTL is a few degrees Celsius above the freezing point from June to December (purple bars in Figs. 7b-d). This can result in larger sea-ice loss for a unit warming than the sea-ice growth for a unit cooling, i.e., asymmetry SIC sensitivities. This is consistent with the SIC responses in the GHG and AER experiments (gray bars in Figs. 7b-c), although the warming for October-December is also larger in the GHG experiment (partly due to the Arctic amplification induced by the larger sea-ice loss). These results imply that the asymmetric responses of Arctic sea ice to CO_2-induced warming and AA-induced cooling, which are closely related to the seasonal evolution of Arctic SIC and Tas, are the main cause of the nonlinear response of Arctic sea ice and temperature in SON.

b. Response of precipitation and the role of moisture

Global-mean precipitation increases with the CO_2 forcing and decreases even more with the AA forcing (Fig. 2c). When combined, they result in considerably less precipitation than in the CTL experiment, in contrast to global-mean Tas, which is slightly above the CTL Tas (Fig. 2b). Further, the global-mean hydrological sensitivity (i.e., the percentage change in precipitation per 1℃ global warming) is 3.64% $℃^{1}$ for the AA forcing and 1.55% $℃^{1}$ for the CO_2 forcing. Thus, the global-mean precipitation is more sensitive to the AA forcing than to the CO_2 forcing, as also noticed previously (e.g., Feichter et al. 2004). This is because aerosols are more effective in changing surface energy fluxes that favor surface evaporation than CO_2 (Feitcher et al. 2004; Lohmann and Feichter 2005). Again, the linear combination of the

Accepted for publication in *Journal of Climate*. DOI10.1175/JCLI-D-19-0195.1.

precipitation changes from the GHG and AA experiments is very close to that from the BOTH experiment (Fig. 2c), suggesting little nonlinear effect for global-mean precipitation. The spatial patterns of the precipitation response are broadly similar among the seasons; thus, we will focus on the precipitation response pattern in JJA when aerosols' impact on precipitation is large in the NH (Fig. 8).

Figures 8a-b show that JJA-mean precipitation responses to the CO_2 and AA forcing are the opposite over much of the globe, except that the AA-induced reduction in precipitation over East and South Asia is much stronger (Fig. 8b) owing to high aerosol emissions and loading there (Fig. 1). Over the tropical Pacific, precipitation increases near the equator and decreases to the north and south of it in the GHG experiment (Fig. 8a), while in the AER experiment (Fig. 8b), precipitation deceases over the equator in both the Pacific and Atlantic and increases to the south of it, which effectively shifts the ITCZ southward, as noticed previously (Ming and Ramaswamy 2009; Allen et al. 2015). Because of the precipitation response to the AA forcing is generally stronger, the precipitation changes in both the combined experiment and the linear combination of the GHG and AER experiments show a pattern that resembles the AER experiment, especially over the NH (Figs. 8c-d), as noticed previously (Wang et al. 2016a). The nonlinear effect on JJA precipitation is insignificant over most of the globe, except East Asia (Fig. 8e). Figure 9a shows that the CO_2 forcing increases summer rainfall over East Asia from about 20°–30°N and slightly decreases it from about 34°–42°N, thereby shifting the East Asian summer rain band southward, while precipitation in East Asia decreases in both the AER and BOTH experiments. Note that the southward shift of the rain band in the GHG experiment may be due to the CO_2-induced SST warming (Chen and Bordoni 2016). The large reduction of the

Accepted for publication in *Journal of Climate*. DOI10.1175/JCLI-D-19-0195.1.

EASM precipitation in the AER experiment likely results from a combination of the changes induced by the local AA forcing and the AA-induced SST changes (Wang et al. 2019). This EASM rainfall reduction differs from the findings of Jiang et al. (2013, 2015), who showed a southward shift of the EASM rain band by AA in simulations using the same model but with prescribed SSTs. However, the nonlinear effect results in less precipitation reduction in the BOTH experiment than the linear combination of the GHG and AER experiments south of 25°N and north of 34°N (Fig. 9a), which acts to offset the CO_2-induced shift. The overall drying over East Asia in the BOTH experiment generally follows that induced by the AA forcing, and changes are all statistically significant (Fig. 9a). In addition, the DJF precipitation response from the nonlinear effect is also small and insignificant over most of the globe, although some significant changes are seen over the eastern equatorial Pacific and North Atlantic (Fig. 8f).

Since monsoon rainfall changes are largely controlled by changes in moisture convergence, mechanisms of the precipitation responses over East Asia are examined using the moisture budget analysis [eq. (8)]. The change in column-integrated mean moisture convergence (δMC) generally agrees well with the rainfall changes for the CO_2 forcing case and the nonlinear effect (Fig. 9b). Note that the AA-induced large rainfall reduction over Southeast Asia cannot be solely explained by the δMC, which may be also related to cloud response (Albrecht 1989; Allen and Sherwood 2010; Jiang et al. 2013; Lau and Kim 2017). Most of the moist convergence change comes from the dynamic component (δDY) (Fig. 9c), with the thermodynamic component (δTH) also being significant from about 25°–39°N but behaving differently in the GHG and AER experiments (Fig. 9d). Overall, most of the JJA precipitation responses over East Asia in the GHG experiment and from the nonlinear effect could be

Accepted for publication in *Journal of Climate*. DOI 10.1175/JCLI-D-19-0195.1.

attributed largely to the mean moisture convergence changes, for which the dynamic component dominates over the thermodynamic component. This implies that the JJA precipitation changes over East Asia are closely related to the low-level circulation changes in this region (not shown), as suggested previously (e.g., Sooraj et al. 2015, 2016).

c. Responses of atmospheric temperature and circulation and the role of aerosol loading

As noticed previously (Wang et al. 2016a), the interhemispheric asymmetric response patterns are unique to the aerosol forcing and absent in the GHG-forced response in the CMIP5 climate models. Similar results are also seen in our CESM1 simulations (not shown). Figures 10a-e show the responses of DJF-mean 500-hPa air temperature (Ta), geopotential height (Z), and horizontal winds. The mid-tropospheric Ta generally increases (decreases) over the globe due to the CO_2 (AA) forcing, but with significant regional variations (Figs. 10a,b). Clearly, the regional cooling patterns for the AER case (Fig. 10b) are related to the aerosol loading patterns shown in Fig. 1c, while the warming patterns for the GHG case (Fig. 10a) are likely related to the surface warming patterns (Fig. 4a) and other processes such as atmospheric diabatic heating (Held et al. 2002). As a result, the mid-tropospheric circulation responses in Z and winds exhibit many regional features, which coincide with the regional Ta response; that is, the largest (smallest) warming induced by the CO_2 forcing yields highest (lowest) Z change, thereby anticyclonic (cyclonic) circulation anomaly (Fig. 10a), while the largest (smallest) cooling induced by the AA forcing yields lowest (highest) Z change, thereby the cyclonic (anticyclonic) circulation anomaly (Fig. 10b). When both forcings are included, the AA-induced tropospheric cooling and the associated Z decrease dominate the NH mid-latitudes, especially over the

Accepted for publication in *Journal of Climate*. DOI10.1175/JCLI-D-19-0195.1.

source region, the North Pacific and the North Atlantic, whereas net tropospheric warming and increased Z are seen over the SH (Fig. 10d). The thermal and circulation response patterns in BOTH resemble those from the linear combination (Fig. 10c) but with reduced magnitudes. As a result, the nonlinear effect (Fig. 10e) shows some regional cooling over North America and Asia, but warming over northern Europe (similar to Fig. 5a for Tas). Significant circulation responses are found mainly over the NH mid-high latitudes (Fig. 10e), such as an anomalous cyclone with colder Ta (relative to CTL) over northeastern North America, and an anomalous anticyclone with warmer Ta over central-northern Europe. In addition, the JJA-mean Ta and circulation responses from the nonlinear effect over the NH are generally weaker and less significant than the DJF-mean responses (Fig. 10f).

What is the possible mechanism that could result in differences between the DJF-mean Ta and circulation response patterns in the BOTH experiment and the linear combination from the GHG and AER experiments? Here, we trace the nonlinear Ta and circulation changes back to the differences between aerosol loading changes in BOTH and AER. In DJF, the aerosol optical depth (AOD) (at 550nm) in the BOTH experiment is higher over central-northern Europe but lower over North America and East Asia than the AER experiment (Fig. 11a), which partially result from the changes in solar absorbing aerosols (Fig. 11b). Thus, the clear-sky SW radiation absorbed by the atmosphere in the BOTH experiment is increased significantly over central-northern Europe relative to the linear combination, which leads to a tropospheric warming there, while tropospheric SW absorption decreases over East Asia and North America that induces a tropospheric cooling over these two regions (Figs. 10e and 11c). Consequently, the nonlinear Ta and circulation response patterns could be largely attributed to the changes of aerosol loading

Accepted for publication in *Journal of Climate*. DOI10.1175/JCLI-D-19-0195.1.

in the BOTH experiment relative to the linear combination, which mainly comes from the AER experiment as there is little AA loading in the GHG experiment (Figs. 12a-b).

In addition, the colder Tas (relative to CTL) over northeastern North America in DJF (Fig. 5a) is largely related to higher SIC over the Hudson Bay (not shown) from the nonlinear effect due to the reduced heating from the ocean. Meanwhile, the higher AOD over central-northern Europe can serve as the cloud condensation nuclei to increase the cloud droplet concentration significantly in this region (Fig. 11e), thereby increasing the total cloud amount (Fig. 11f) due to the aerosol indirect effect (Albrecht 1989). Land-atmosphere interactions may also play a role in affecting the cloud droplet formation (Shepherd 2005), including the effect from land surface heterogeneity (Lee et al. 2019). Thus, the land surface may also have contributed to the nonlinear changes of cloud droplet concentrations over central-northern Europe. Furthermore, the increased total cloud amount in the nonlinear effect over central Europe and North America is also related to increased lower-tropospheric water content and anomalous upward motion in BOTH relative to the linear combination (not shown). As a result, more clouds over central-northern Europe in BOTH (relative to the linear combination) would increase the LW surface cloud forcing (i.e., a greenhouse effect; Fig. 11g) while the increase in cloud SW cooling effect is small (Fig. 11h), thus contributing to a warmer Tas (relative to CTL; Fig. 5a) in this region. Note that the LW (SW) surface cloud forcing here is defined as the difference between the all-sky and clear-sky net surface LW (SW) radiation (positive downward; Ramanathan et al. 1989). Besides, the warmer (colder) troposphere over central-northern Europe (northeastern North America) also acts to enhance (reduce) the downward LW radiation to further warm (cool) the surface in the nonlinear effect. Overall, the increased downward LW radiation at the surface

Accepted for publication in *Journal of Climate*. DOI10.1175/JCLI-D-19-0195.1.

(Fig. 11d), which may come from a warmer troposphere (Fig. 10e) and a higher greenhouse effect by more clouds (Fig. 11g), is a key factor for the surface warming over central-northern Europe in DJF (Fig. 5a).

Thus, one may wonder how the AOD over central-northern Europe would increase in BOTH relative to AER since the same aerosol emissions are applied in BOTH and AER. In the AER experiment, the European aerosols increase substantially in DJF (Fig. 12a), which is partially advected northeastward to East Asia by the prevailing southwesterly winds in the lower troposphere. When the CO_2 forcing is added into the ARE experiment (i.e., the BOTH experiment), significant northeasterly wind anomalies are seen in the lower troposphere over central-northern Europe (Fig. 12b), which weakens the prevailing southwesterly and thus the export of European aerosols in BOTH. As a result, more aerosols accumulate over Europe in BOTH (Fig. 11a) than AER, leading to a higher AOD. The relationship between the CO_2-induced change of low-level zonal wind and nonlinear changes of AOD and Tas over central-northern Europe are shown in Figs. 12c-d, respectively. Nonlinear changes of AOD (Tas) are significantly anti-correlated with the low-level zonal wind change in the GHG experiment with a correlation coefficient of -0.7 (-0.62). This suggests that relative to CTL, the reduced low-level westerly winds induced by the CO_2 forcing leads to higher aerosol loading over central-northern Europe in BOTH that acts to heat the atmosphere in DJF via absorbing SW radiation and warm the surface due to increased downward LW radiation, resulting in some nonlinear thermal responses and thereby circulation responses.

4. Conclusions and discussion

Accepted for publication in *Journal of Climate*. DOI10.1175/JCLI-D-19-0195.1.

In this study, we have performed and analyzed a set of CESM1 experiments to examine the nonlinear climate response, defined as the deviation from the linear combination of the responses in the individual forcing runs, to increasing CO_2 and AA, focusing on the spatial and seasonal characteristics and possible causes. The experiments include a case with CO_2 forcing only (GHG), a case with AA forcing only (AER), and a case with both the CO_2 and AA forcing globally (BOTH). The global-mean responses of TOA radiative fluxes, surface air temperature (Tas) and precipitation to the combined forcing are very close to the linear combination of the responses to the CO_2 and AA forcing alone, leading to small nonlinear effects on global-mean Tas and precipitation. However, significant nonlinear climate responses are seen over certain regions during some seasons.

Significant nonlinear Tas changes are seen over the Arctic Ocean in SON and over Europe and North America in DJF. The Arctic surface warming in BOTH is considerably smaller than the linear combination of the Tas changes from GHG and AER in SON, indicating an Arctic cooling due to the nonlinear effect. This reduced Arctic warming is caused by more Arctic sea-ice concentration (SIC) in BOTH than the linear combination of SIC from GHG and AER via reduced upward LW radiation and turbulent fluxes in SON. This nonlinear SIC change comes from the asymmetric responses of Arctic SIC to CO_2-induced warming and AA-induced cooling, which are closely related to the seasonal evolution of Arctic SIC and Tas. Specifically, there are more Arctic oceanic areas that are just a few degrees Celsius below the freezing point than the areas that are a few degrees Celsius above the freezing point, leading to higher SIC sensitivity to warming than to cooling, and this SIC sensitivity asymmetry leads to less sea-ice loss in BOTH (as the AA forcing cancels much of the CO_2-induced warming) than the linear

Accepted for publication in *Journal of Climate*. DOI10.1175/JCLI-D-19-0195.1.

combination of the SIC changes from GHG and AER (as the same amount of warming causes more sea-ice loss in GHG than the sea-ice gain in AER). The colder Arctic Tas would further increase the sea-ice cover, which in turn would lead to colder Tas, forming a positive feedback.

However, the nonlinear warming over central-northern Europe in DJF is mainly caused by the higher aerosol loading and increased greenhouse effect by more clouds in BOTH relative to AER. The lower-tropospheric northeasterly wind anomalies induced by the CO_2 forcing weakens the export of European aerosols when both forcings are included, leading to higher aerosol loading over central-northern Europe in BOTH than in AER, especially for solar absorbing aerosols. The increased AOD leads to more clouds and a higher greenhouse effect by clouds (and the warmer troposphere), and thus a warmer surface over Europe.

The spatial pattern of precipitation response to combined forcing resembles that to the AA forcing, which is broadly similar among all seasons. Nonlinear effects on precipitation are small over most of the globe, except over East Asia in JJA. Positive precipitation anomalies from the nonlinear effect are found north of ~34°N over East Asia in JJA, while negative anomalies are seen south of ~25°N. This nonlinear precipitation response pattern shifts the East Asian summer rain band northward, which compensates the CO_2-induced shift. A moisture budget analysis further revealed that most of the East Asian summer precipitation responses to the CO_2 forcing and from the nonlinear effects can be explained by the mean moisture convergence changes (which implies a small impact from aerosol indirect effect on clouds), for which the dynamic component dominates over the thermodynamic component.

The DJF-mean response of mid-tropospheric air temperature (Ta) and circulation to the combined forcing resembles that from the linear combination in spatial pattern but with smaller

Accepted for publication in *Journal of Climate*. DOI10.1175/JCLI-D-19-0195.1.

magnitude. This results in some significant nonlinear responses over central-northern Europe (warming and anticyclonic) and northeastern North America and central-eastern Asia (cooling and cyclonic) in DJF. The lower troposphere over central-northern Europe (East Asia and North America) absorbs more (less) SW radiation in BOTH than the linear combination due to the higher (lower) absorbing aerosol loading, thus the nonlinear effect acts to warm (cool) the troposphere and induce anomalous anticyclonic (cyclonic) circulation over the regions. Generally, the nonlinear effect on Ta and atmospheric circulation acts to partially weaken the linear combination of the responses to individual forcings. Overall, the regional circulation responses to the individual and combined forcing agree well with the regional Ta responses, with the largest (smallest) warming regions corresponding to the largest (smallest) increase in geopotential height and thus anticyclonic (cyclonic) circulation response.

This study highlights the important role of nonlinear climate responses to the CO_2 and AA forcing in shaping the seasonal and regional responses. The main nonlinear responses and related processes include SON Tas and SIC changes over the Arctic and DJF Tas changes over Europe and northeastern North America. For the annual- and zonal-mean climate responses, our results are consistent with previous studies (e.g., Feichter et al. 2004; Ming and Ramaswamy 2009; Ming et al. 2011), which only examined annual-mean responses, in that the surface warming is smaller in the combined forcing simulation than the linear combination of the individual responses, especially over the Northern Hemisphere high latitudes. However, we found that the nonlinear response occurs mainly over the extratropical hemisphere during the winter and autumn seasons, while it is small in the low latitudes. Previous studies (Feichter et al. 2004; Ming and Ramaswamy 2009; Ming et al. 2011) have discussed the causes of the large

Accepted for publication in *Journal of Climate*. DOI10.1175/JCLI-D-19-0195.1.

nonlinear response in annual-mean surface temperature over the northern high latitudes, which occurs only over the Arctic in SON based on our analysis (Fig. 5d); they attributed it to cloud response (Feichter et al. 2004), surface albedo feedback (Ming and Ramaswamy 2009) and tropopause height change (Ming et al. 2011). In contrast, we found that the asymmetric Arctic sea-ice sensitivity to the CO_2-induced warming and the AA-induced cooling plays a primary role in damping the surface warming in the BOTH experiment. In addition, Feichter et al. (2004) suggested that the increase in GHGs may alter the aerosol loading via the aerosol-temperature feedback. Here we found that atmospheric aerosols can also be redistributed by the CO_2-induced circulation changes (Fig. 12), which is important for the nonlinear response in DJF over Europe and North America (Fig. 5a).

Although internal variability is reduced to about 8% of that in the original fields in our 150-averaged data analyzed here, it may still induce slight differences at the grid box level among the averaged fields from the CTL, BOTH, GHG and AER experiments that are unrelated to the forced response, and thus may increase the uncertainty in our estimated nonlinear effect. However, the effect of internal variability in our regionally- and globally-averaged changes is likely negligible as the spatial averaging would further reduce internal variations substantially. On the other hand, large uncertainties still remain among models in simulating aerosol radiative forcing and the resultant climate responses (Myhre et al. 2013), and the aerosol forcing may also modulate the internal (ocean driven) variability (e.g., Booth et al. 2012; Boo et al. 2015) and its impacts on the atmosphere (e.g., Kim et al. 2016). Thus, the changed aerosol loading in BOTH (relative to AER) may also induce nonlinear response via modulating the internal variability. These uncertainties present difficulties and challenges in reliably assessing the

Accepted for publication in *Journal of Climate*. DOI 10.1175/JCLI-D-19-0195.1.

nonlinear climate responses to the CO_2 and AA forcing. However, the nonlinear aspects examined here are based on CESM1 only; it would be interesting to see whether similar processes exist in other models. Thus, further studies are still needed using multiple models to examine the nonlinear responses and underlying mechanisms.

Acknowledgements This work was jointly supported by the National Natural Science Foundation of China (41705054 and 41575077), Natural Science Foundation of Jiangsu Province (BK20170942), General Program of Natural Science Research of Jiangsu Province University (17KJB170012), Startup Foundation for Introducing Talent of NUIST (2016r051), Priority Academic Program Development of Jiangsu Higher Education Institutions (PAPD), and China Scholarship Council (201808320137). A. Dai was supported by the National Science Foundation (AGS-1353740 and OISE-1743738), the U.S. Department of Energy's Office of Science (DE-SC0012602), and the U.S. National Oceanic and Atmospheric Administration (NA15OAR4310086).

Accepted for publication in *Journal of Climate*. DOI10.1175/JCLI-D-19-0195.1.

References

Albrecht, B., 1989: Aerosols, cloud microphysics, and fractional cloudiness. *Science*, **245**, 1227–1230, doi:10.1126/science.245.4923.1227.

Allen, R. J., and S. C. Sherwood, 2010: Aerosol-cloud semi-direct effect and land-sea temperature contrast in a GCM. *Geophys. Res. Lett.*, **37**, L07702, doi:10.1029/2010GL042759.

Allen, R. J., A. T. Evan, and B. B. Booth, 2015: Interhemispheric aerosol radiative forcing and tropical precipitation shifts during the late twentieth century. *J. Climate*, **28**, 8219–8246, doi:10.1175/JCLI-D-15-0148.1.

Barnes, E.A., and L. M. Polvani, 2015: CMIP5 projections of Arctic amplification, of the North American/North Atlantic circulation, and of their relationship. *J. Climate*, **28**, 5254–5271, doi:10.1175/JCLI-D-14-00589.1.

Boo, K.-O., B. B. B. Booth, Y.-H. Byun, J. Lee, C. H. Cho, S. Shim, and K.-T. Kim, 2015: Influence of aerosols in multidecadal SST variability simulations over the North Pacific, *J. Geophys. Res. Atmos.*, **120**, 517–531, doi:10.1002/2014JD021933.

Booth, B., N. J. Dunstone, P. R. Halloran, T. Andrews, and N. Bellouin, 2012: Aerosols implicated as a prime driver of twentieth-century North Atlantic climate variability. *Nature*, **484**, 228–232, doi:10.1038/nature10946.

Chen, J., and S. Bordoni, 2016: Early summer response of the East Asian summer monsoon to atmospheric CO2 forcing and subsequent sea surface warming. *J. Climate*, **29**, 5431–5446, doi:10.1175/JCLI-D-15-0649.1.

Chen, G., W.-C. Wang, and J.-P. Chen, 2018: Circulation responses to regional aerosol climate forcing in summer over East Asia. *Climate Dyn.*, **51**, 3973–3984, doi:10.1007/s00382-

Accepted for publication in *Journal of Climate*. DOI10.1175/JCLI-D-19-0195.1.

018-4267-3.

Clement, A. C., R. Seager, M. A. Cane, and S. E. Zebiak, 1996: An ocean dynamical thermostat. *J. Climate*, **9**, 2190–2196, doi:10.1175/1520-0442(1996)009<2190:AODT>2.0.CO;2.

Collins, M., S. An, W. Cai, A. Ganachaud, E. Guilyardi, F. F. Jin, M. Jochum, M. Lengaigne, S. Power, A. Timmermann, G. Vecchi, and A. Wittenberg, 2010: The impact of global warming on the tropical Pacific Ocean and El Nino. *Nat. Geosci.*, **3**, 391–397, doi:10.1038/ngeo868.

Dai, A., H. Li, Y. Sun, L.-C. Hong, LinHo, C. Chou, and T. Zhou, 2013: The relative roles of upper and lower tropospheric thermal contrasts and tropical influences in driving Asian summer monsoons. *J. Geophys. Res. Atmos.*, **118**, 7024–7045, doi:10.1002/jgrd.205065.

Dai, A., D. Luo, M. Song, and J. Liu, 2019: Arctic amplification is caused by sea-ice loss under increasing CO_2. *Nat. Commun.*, **10**, 121, doi:10.1038/s41467-018-07954-9.

Dee, D. P., S. M. Uppala, A. J. Simmons, et al., 2011: The ERA- Interim reanalysis: configuration and performance of the data assimilation system. *Q. J. Royal Metero. Soc.*, **137**, 553–597, doi:10.1002/qj.828.

Deng, J., and H. Xu, 2016: Nonlinear effect on the East Asian summer monsoon due to two coexisting forcing factors in eastern China: an AGCM study. *Climate Dyn.*, **46**, 3767–3784, doi:10.1007/s00382-015-2803-y.

Deser, C., R. Tomas, M. Alexander, and D. Lawrence, 2010: The seasonal atmospheric response to projected Arctic sea ice loss on the late twenty-first century. *J. Climate*, **23**, 333–351, doi:10.1175/2009JCLI3053.1.

Feichter, J., E. Roeckner, U. Lohmann, and B. Liepert, 2004: Nonlinear Aspects of the Climate

Accepted for publication in *Journal of Climate*. DOI10.1175/JCLI-D-19-0195.1.

Response to Greenhouse Gas and Aerosol Forcing. *J. Climate*, **17**, 2384–2398, doi:10.1175/1520-0442(2004)017<2384:NAOTCR>2.0.CO;2.

Gagné, M.-È., J. C. Fyfe, N. P. Gillett, I. V. Polyakov, and G. M. Flato, 2017: Aerosol-driven increase in Arctic sea ice over the middle of the twentieth century. *Geophys. Res. Lett.*, **44**, 7338–7346, doi:10.1002/2016GL071941.

Ganguly, D., P. J. Rasch, H. Wang, and J. Yoon, 2012: Fast and slow respones of the South Asian monsoon system to anthropogenic aerosols. *Geophys. Res. Lett.*, **39**, L18804, doi:10.1029/2012GL053043.

Held, I. M., and B. J. Soden, 2006: Robust responses of the hydrological cycle to global warming. *J. Climate*, **19**, 5686–5699, doi:10.1175/JCLI3990.1.

Held, I., M. Ting, and H. Wang, 2002: Northern winter stationary waves: Theory and modeling. *J. Climate*, **15**, 2125–2144, doi:10.1175/1520-0442(2002)015<2125:NWSWTA>2.0.CO;2

Holland, M. M. and C. M. Bitz, 2003: Polar amplification of climate change in coupled models. *Climate Dyn.*, **21**, 221–232, doi:10.1007/s00382-003-0332-6.

Hurrell, J. W., et al., 2013: The community earth system model: A framework for collaborative research. *Bull. Amer. Meteor. Soc.*, **94**, 1339–1360, doi:10.1175/BAMS-D-12-00121.1.

Jiang, Y., X. Liu, X. Q. Yang, and M. Wang, 2013: A numerical study of the effect of different aerosol types on East Asian summer clouds and precipitation. *Atmos. Environ.*, **70**, 51–63, doi:10.1016/j.atmosenv.2012.12.039.

Jiang, Y., X. Q. Yang, and X. Liu, 2015: Seasonality in anthropogenic aerosol effects on East Asian climate simulated with CAM5. *J. Geophys. Res. Atmos.*, **120**, 10837–10861, doi: 10.1002/2015JD023451.

Accepted for publication in *Journal of Climate*. DOI 10.1175/JCLI-D-19-0195.1.

Kejellsson, J., 2015: Weakening of the global atmospheric circulation with global warming. *Climate Dyn.*, **45**, 975–988, doi:10.1007/s00382-014-2337-8.

Kim, M. K., K. M. Lau, M. Chin, K. M. Kim, Y. C. Sud, and G. K. Walker, 2006: Atmospheric teleconnection over Eurasia induced by aerosol radiative forcing during boreal spring. *J. Climate*, **19**, 4700–4718, doi:10.1175/JCLI3871.1.

Kim, M. K., W. Lau, K. M. Kim, J. Sang, Y. H. Kim, and W. S. Lee, 2016: Amplification of ENSO effects on Indian summer monsoon by absorbing aerosols. *Climate Dyn.*, **46**, 2657–2671, doi:10.1007/s00382-015-2722-y.

Lamarque, J. F., et al., 2010: Historical (1850–2000) gridded anthropogenic and biomass burning emissions of reactive gases and aerosols: methodology and application. *Atmos. Chem. Phys.*, **10**, 7017–7039, doi:10.5194/acp-10-7017-2010.

Lau, K. M., M. K. Kim, and K. M. Kim, 2006: Asian summer monsoon anomalies induced by aerosol direct forcing: The role of the Tibetan Plateau. *Climate Dyn.*, **26**, 855–864, doi: 10.1007/s00382-006-0114-z.

Lau, W. K.-M., and K. M. Kim, 2017: Competing influences of greenhouse warming and aerosols on Asian summer monsoon circulation and rainfall. *Asia-Pacific, J. Atmos. Sci.*, **53**, 181–194, doi:10.1007/s13143-017-0033-4.

Lee, J. M., Y. Zhang, and S. A. Klein, 2019: The effect of land surface heterogeneity and background wind on shallow cumulus clouds and the transition to deeper convection. *J. Atmos. Sci.*, **76**, 401–419, doi:10.1175/JAS-D-18-0196.1.

Lewinschal, A., A. K. L. Ekman, and H. Körnich, 2013: The role of precipitation in aerosol-induced changes in northern hemisphere wintertime stationary waves. *Climate Dyn.*, **41**,

Accepted for publication in *Journal of Climate*. DOI10.1175/JCLI-D-19-0195.1.

647–661, doi:10.1007/s00382-012-1622-7.

Li, H., A. Dai, T. Zhou, and J. Lu, 2010: Response of East Asian summer monsoon to historical SST and atmospheric forcing during 1950-2000. *Climate Dyn.*, **34**, 501–514, doi:10.1007/s00382-008-0482-7.

Li, X., M. Ting, C. Li, and N. Henderson, 2015: Mechanisms of Asian summer monsoon changes in response to anthropogenic forcing in CMIP5 models. *J. Climate*, **28**, 4107–4125, doi:10.1175/JCLI-D-14-00559.1.

Lohmann, U., and J. Feichter, 2005: Global indirect aerosol effects: A review. *Atmos. Chem. Phys.*, **5**, 715–737, doi:10.5194/acp-5-715-2005.

Menon, S., J. Hansen, L. Nazarenko, and Y. Luo, 2002: Climate effects of black carbon aerosols in China and India. *Science*, **297**, 2250–2253, doi:10.1126/science.1075159.

Ming, Y., and V. Ramaswamy, 2009: Nonlinear climate and hydrological responses to aerosol effects. *J. Climate*, **22**, 1330–1339, doi:10.1175/2008JCLI2362.1.

Ming, Y., and V. Ramaswamy, 2011: A model investigation of aerosol-induced changes in tropical circulation. *J. Climate*, **24**, 5125–5133, doi:10.1175/2011JCLI4108.1.

Ming, Y., V. Ramaswamy, and G. Chen, 2011: A model investigation of aerosol-induced changes in boreal winter extratropical circulation. *J. Climate*, **24**, 6077–6091, doi:10.1175/2011JCLI4111.1.

Myhre, G., and Coauthors, 2013: Anthropogenic and natural radiative forcing. *Climate Change 2013: The Physical Science Basis*, T. F. Stocker et al., Eds., Cambridge University Press, 659–740, doi:10.1017/CBO9781107415324.018.

Neale, R. B., et al., 2012: Description of the NCAR Community Atmosphere Model (CAM5.0),

Accepted for publication in *Journal of Climate*. DOI10.1175/JCLI-D-19-0195.1.

NCAR Tech. 650 Note, NCAR/TN-4861STR, 274 pp., *Natl. Cent. for Atmos. Res*.

Ramanathan, V., R. D. Cess, E. F. Harrison, P. Minnis, B. R. Barkstrom, E. Ahmad, and D. Hartman, 1989: Cloud–radiative forcing and climate: Results for the Earth Radiation Budget Experiment. *Science*, **243**, 57–63, doi: 10.1126/science.243.4887.57.

Rotstayn, L. D., and U. Lohmann, 2002: Tropical rainfall trends and the indirect aerosol effect. *J. Climate*, **15**, 2103–2116, doi: 10.1175/1520-0442(2002)015<2103:TRTATI>2.0.CO;2.

Serreze, M.C., and R. G. Barry, 2011: Processes and impacts of Arctic amplification: A research synthesis. *Global and Planetary Change*, **77**, 85–96, doi:10.1016/j.gloplacha.2011.03.004.

Screen, J. A., and I. Simmonds, 2010: The central role of diminishing sea-ice in recent Arctic temperature amplification. *Nature*, **464**, 1334–1337, doi:10.1038/nature09051.

Shepherd, J. M., 2005: A review of current investigations of urban-induced rainfall and recommendations for the future. *Earth Interact.*, **9**, 1–27, doi:10.1175/EI156.1.

Song, F., T. Zhou, and Y. Qian, 2014: Responses of East Asian summer monsoon to natural and anthropogenic forcings in the 17 latest CMIP5 models. *Geophys. Res. Lett.*, **41**, 596–603, doi:10.1002/2013GL058705.

Sooraj, K. P., P. Terray, and M. Mujumdar, 2015: Global warming and the weakening of the Asian summer monsoon circulation: assessments from the CMIP5 models. *Climate Dyn.*, **45**, 233–252, doi:10.1007/s00382-014-2257-7.

Sooraj, K. P., P. Terray, and P. Xavier, 2016: Sub-seasonal behavior of Asian summer monsoon under a changing climate: assessments using CMIP5 models. *Climate Dyn.*, **46**, 4003–4025, doi:10.1007/s00382-015-2817-5.

Accepted for publication in *Journal of Climate*. DOI10.1175/JCLI-D-19-0195.1.

Sun, Y., Y. Ding, and A. Dai, 2010: Changing links between South Asian summer monsoon circulation and tropospheric land–sea thermal contrasts under a warming scenario. *Geophys. Res. Lett.*, **37**, L02704, doi:10.1029/2009GL041662.

Sutton, R. T., B. Dong, and J. M. Gregory, 2007: Land/sea warming ratio in response to climate change: IPCC AR4 model results and comparison with observations. *Geophys. Res. Lett.*, **34**, L02701, doi:10.1029/2006GL028164.

Taylor, K. E., R. J. Stouffer, and G. A. Meehl, 2012: An Overview of CMIP5 and the Experiment Design. *B. Am. Meteorol. Soc*., **93**, 485–498, doi:10.1175/bams-d-11-00094.1.

Tian, F., B. Dong, J. Robson, and R. Sutton, 2018: Forced decadal changes in the East Asian summer monsoon: the roles of greenhouse gases and anthropogenic aerosols. *Climate Dyn.*, **51**, 3699–3715, doi:10.1007/s00382-018-4105-7.

Twomey, S., 1974: Pollution and the planetary albedo. *Atmos. Envir.*, **8**, 1251–1256, doi:10.1016/0004-6981(74)90004-3.

Vecchi, G. A., and B. J. Soden, 2007: Global warming and the weakening of the tropical circulation. *J. Climate*, **20**, 4316–4340, doi:10.1175/JCLI4258.1.

Wang, H., S.-P. Xie, and Q. Liu, 2016a: Comparison of Climate Response to Anthropogenic Aerosol versus Greenhouse Gas Forcing: Distinct Patterns. *J. Climate*, **29**, 5175–5188, doi: 10.1175/JCLI-D-16-0106.1.

Wang, H., S.-P. Xie, H. Tokinaga, Q. Liu, and Y. Kosaka, 2016b: Detecting cross-equatorial wind change as a fingerprint of climate response to anthropogenic aerosol forcing. *Geophys. Res. Lett.*, **43**, 3444–3450, doi:10.1002/2016GL068521.

Wang, H., S.-P. Xie, Y. Kosaka, Q. Liu, and Y. Du, 2019: Dynamics of Asian summer monsoon

Accepted for publication in *Journal of Climate*. DOI10.1175/JCLI-D-19-0195.1.

response to anthropogenic aerosol forcing. *J. Climate*, **32**, 843–858, doi:10.1175/JCLI-D-18-0386.1.

Wang, Z., H. Zhang, X. Jing, and X. Wei, 2013: Effect of non-spherical dust aerosol on its direct radiative forcing. *Atmos. Res.*, **120–121**, 112–126, doi:10.1016/j.atmosres.2012.08.006.

Williams, K. D., A. Jones, D. L. Roberts, C. A. Senior, and M. J. Woodage, 2001: The response of the climate system to the indirect effects of anthropogenic sulfate aerosol. *Climate Dyn.*, **17**, 845–856, doi: 10.1007/s003820100150.

Wu, L., H. Su, and J. H. Jiang, 2013: Regional simulation of aerosol impacts on precipitation during the East Asian summer monsoon. *J. Geophys. Res. Atmos*., **118**, 6454–6467, doi:10.1002/ jgrd.50527.

Xie, S.-P., B. Lu, and B. Xiang, 2013: Similar spatial patterns of climate responses to aerosol and greenhouse gas changes. *Nat. Geosci.*, **6**, 828–832, doi:10.1038/ngeo1931.

Yeh, S. W., W. M. Kim, Y. H. Kim, B. K. Moon, R. J. Park, and C. K. Song, 2013: Changes in the variability of the North Pacific sea surface temperature caused by direct sulfate aerosol forcing in China in a coupled general circulation model, *J. Geophys. Res. Atmos.*, **118**, 1261–1270, doi:10.1029/2012JD017947.

Zhang, L., and T. Li, 2016: Relative roles of anthropogenic aerosols and greenhouse gases in land and oceanic monsoon changes during past 156 years in CMIP5 models. *Geophys. Res. Lett.*, **43**, 5295–5301, doi:10.1002/2016GL069282.

Zhang, L., and T. Li, 2017: Relative roles of differential SST warming, uniform SST warming and land surface warming in determining the Walker circulation changes under global warming. *Climate Dyn.*, **48**, 987–997, doi: 10.1007/s00382-016-3123-6.

Accepted for publication in *Journal of Climate*. DOI10.1175/JCLI-D-19-0195.1.

Table 1. Numerical experiments and climate response signals used in this study.

Name	CO_2 level	AA emission	Climatic signals
CTL	Year 1850	Year 1850	/
GHG	Year 2000	Year 1850	GHG – CTL (*CO_2 effect*)
AER	Year 1850	Year 2000	AER – CTL (*Aerosol effect*)
BOTH	Year 2000	Year 2000	BOTH – CTL (*Combined effect*)

Accepted for publication in *Journal of Climate*. DOI 10.1175/JCLI-D-19-0195.1.

Table 2. Global-mean and annual-mean changes of the net shortwave (SW) flux (positive downward, $W{\cdot}m^{-2}$) at the top-of-the-atmosphere (TOA) and total cloud amount (%). The cloudy-sky flux is defined as the difference between all-sky and clear-sky fluxes.

	GHG – CTL	AER – CTL	BOTH – CTL
All-sky net SW flux at TOA	0.82	-2.76	-1.95
Clear-sky net SW flux at TOA	0.69	-0.77	-0.05
Cloudy-sky net SW flux at TOA	0.13	-1.99	-1.90
Total cloud amount	-0.33	0.74	0.40

Accepted for publication in *Journal of Climate*. DOI10.1175/JCLI-D-19-0195.1.

Figure captions

Figure 1. Spatial distribution of (a) anthropogenic aerosol surface emissions ($\times 10^{10}$ mol·cm^{-2}·s^{-1}) at year 1850 used in CTL, (b) same as (a) except for year 2000 used in the AER or BOTH experiment, and (c) changes of aerosol optical depth (AOD, $\times 10^{-2}$) at 550nm in AER with respect to CTL. Only changes statistically significant at the 95% confidence level are plotted in (c) based on a Student's *t* test.

Figure 2. Time series of 11-year smoothed global-mean annual (a) net radiation flux at the top of the atmosphere (TOA, positive downward, W·m^{-2}), (b) surface air temperature (Tas, ℃), and (c) precipitation (mm·day^{-1}) from each of the experiments and the linear combination of CTL and changes from the GHG and AER experiments [i.e., CTL+ (GHG – CTL) + (AER – CTL), red line].

Figure 3. Time series of 11-year smoothed global-mean annual changes (relative to CTL) of (a) net radiation flux at TOA (positive downward, W·m^{-2}), (b) net longwave (LW) flux at TOA (positive upward, W·m^{-2}), and (c) net shortwave (SW) flux at TOA (positive downward, W·m^{-2}) due to the CO_2 forcing (GHG – CTL, orange line), aerosol forcing (AER – CTL, blue line), their linear combination (GHG – CTL + AER – CTL, red line), and the combined forcing (BOTH – CTL, black line).

Figure 4. Seasonal-mean changes of surface air temperature (Tas, ℃) due to the (a-d) CO_2 forcing (GHG – CTL), (e-h) aerosol forcing (AER – CTL), and (i-l) the combined forcing (BOTH – CTL) for the four seasons: (a, e, i) DJF, (b, f, j) MAM, (c, g, k) JJA, and (d, h, l) SON. The stippling indicates the changes are statistically significant at the 95% confidence level

Accepted for publication in *Journal of Climate*. DOI10.1175/JCLI-D-19-0195.1.

based on a Student's *t* test. The spatial correlation coefficients between the linear combination of Tas responses to the individual forcings and the Tas response to the combined forcing for the four seasons are given at the top center of (i-l), respectively.

Figure 5. Seasonal-mean changes of Tas (℃) due to the nonlinear effect [i.e., (BOTH – CTL) – (GHG – CTL + AER – CTL)]: (a) DJF, (b) MAM, (c) JJA and (d) SON. The stippling indicates the changes are statistically significant at the 95% confidence level based on a Student's *t* test.

Figure 6. SON-mean changes of (a) Tas (℃), (b) sea ice concentration (SIC, % of area), (c) surface upward longwave (LW_up, $W \cdot m^{-2}$), and (d) turbulent (sensible + latent) heat flux (positive upward, $W \cdot m^{-2}$) due to the nonlinear effect. The stippling indicates the changes are statistically significant at the 95% confidence level based on a Student's *t* test.

Figure 7. 150-yr mean annual cycle of SIC (grey bars, left y-axis, %) and Tas (red curves, right y-axis, ℃) averaged over the Arctic (70°–90°N) from (a) CTL and their changes due to the (b) CO_2 forcing (GHG – CTL), (c) aerosol forcing (AER – CTL), (d) their linear combination (i.e., b + c), (e) the combined forcing (BOTH – CTL), and (f) the nonlinear effect (i.e., e – d). The green curves in (b-d) indicate the SIC response to 1℃ warming or cooling, and the purple bars indicate the *potential* SIC responses diagnosed using Tas in CTL (see eqs. 6-7 in section 2c). The blue bars in (e, f) indicate the *inferred* SIC responses to the combined and nonlinear effects based on eqs. 4-5 in section 2c, respectively.

Figure 8. JJA-mean changes of precipitation ($mm \cdot day^{-1}$) due to the (a) CO_2 forcing (GHG – CTL), (b) aerosol forcing (AER – CTL), (c) their linear combination (i.e., a + b), (d) combined forcing (BOTH – CTL), and (e) the nonlinear effect (i.e., d – c). (f) Same as (e) except for DJF.

Accepted for publication in *Journal of Climate*. DOI10.1175/JCLI-D-19-0195.1.

The stippling indicates the changes are statistically significant at the 95% confidence level based on a Student's *t* test.

Figure 9. JJA-mean changes of (a) precipitation (mm·day^{-1}), (b) mean moisture convergence (mm·day^{-1}), and its (c) dynamic component (mm·day^{-1}) and (d) thermodynamic component (mm·day^{-1}) zonally averaged over East Asia (105°–120°E). The gray dashed line in (a) denotes the JJA-mean precipitation in CTL, which is scaled by 1/10 in order to use the same y-axis. Circles in (a) indicate the changes are statistically significant at the 95% confidence level based on a Student's *t* test.

Figure 10. DJF-mean changes of 500-hPa air temperature (shading; ℃), geopotential height (contours; gpm), and horizontal winds (vectors; m·s^{-1}) due to the (a) CO_2 forcing (GHG – CTL), (b) aerosol forcing (AER – CTL), (c) their linear combination (i.e., a + b), (d) the combined forcing (BOTH – CTL), and (e) the nonlinear effect (i.e., d – c). (f) Same as (e) except for JJA. The contour interval is 4 gpm, and the zero contour is omitted for clarity. Both stippling and vectors indicate the changes are statistically significant at the 95% confidence level based on a Student's *t* test.

Figure 11. DJF-mean nonlinear changes of (a) aerosol optical depth (AOD) at 550nm (×10^{-3}), (b) AOD at 550nm for absorbing aerosols (×10^{-4}), (c) clear-sky net shortwave radiation absorbed by the atmosphere (W·m^{-2}), (d) surface downward LW (W·m^{-2}), (e) cloud droplet concentration (×10^{9}·m^{-2}), (f) total cloud amount (% of area), (g) LW and (h) SW surface cloud forcing (W·m^{-2}, positive downward). The LW (SW) surface cloud forcing is defined as the difference between the all-sky and clear-sky net surface LW (SW) radiation (Ramanathan et al.

Accepted for publication in *Journal of Climate*. DOI10.1175/JCLI-D-19-0195.1.

1989). A positive (negative) surface cloud forcing indicates that clouds enhance (reduce) the downward LW or SW at the surface, leading to a surface warming (cooling) effect. The stippling indicates the changes are statistically significant at the 95% confidence level based on a Student's *t* test. The green rectangle indicates central-northern Europe (0°–60°E, 50°–70°N).

Figure 12. Spatial distributions of DJF-mean (a) AOD changes (shading, $\times10^{-2}$) in AER relative to CTL, and climatological mean 925-hPa horizontal winds in AER (vectors, $m \cdot s^{-1}$) and (b) AOD changes (shading, $\times10^{-2}$) and 925-hPa horizontal wind anomalies (vectors, $m \cdot s^{-1}$) in GHG relative to CTL. Only changes statistically significant at the 95% confidence level are plotted in (a-b) based on a Student's *t* test. The red rectangle indicates central-northern Europe (0°–60°E, 50°–70°N). (c) Scatter plot of 925-hPa zonal wind change due to the CO_2 forcing (x-axis, $m \cdot s^{-1}$) and nonlinear AOD at 550nm change (y-axis, $\times10^{-2}$) in DJF averaged over central-northern Europe. (d) Same as (c), except for 925-hPa zonal wind change due to the CO_2 forcing (x-axis, $m \cdot s^{-1}$) and nonlinear Tas change (y-axis, ℃). In (c-d), each circle indicates a model year, the red line indicates the regression line, and the regression equation and the correlation coefficient are given at the top right corner.

Accepted for publication in *Journal of Climate*. DOI10.1175/JCLI-D-19-0195.1.

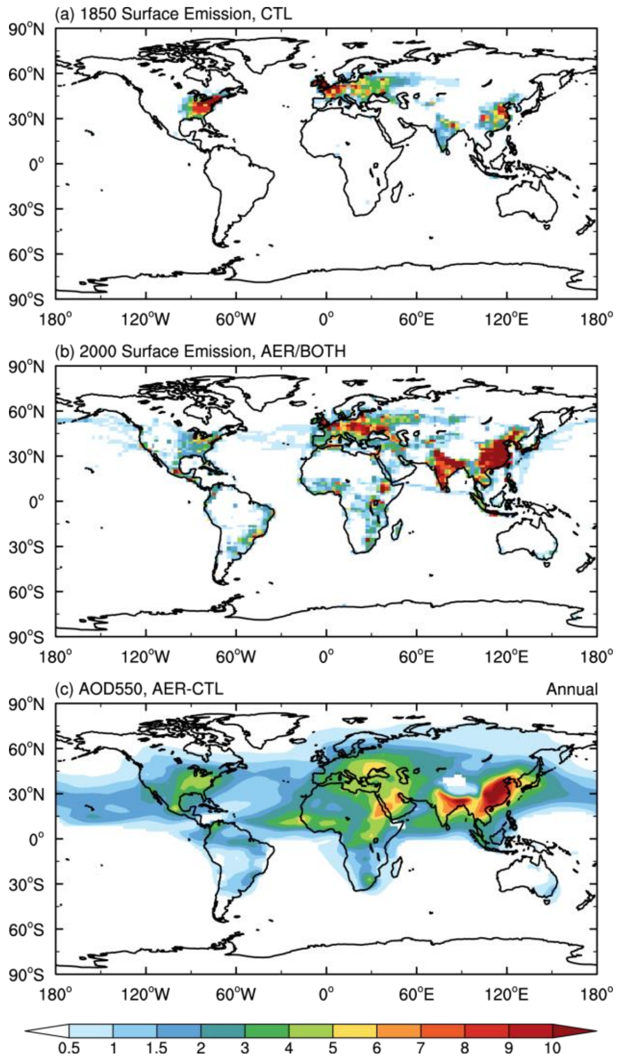

Figure 1. Spatial distribution of (a) anthropogenic aerosol surface emissions ($\times 10^{10}$ mol·cm^{-2}·s^{-1}) at year 1850 used in CTL, (b) same as (a) except for year 2000 used in the AER or BOTH experiment, and (c) changes of aerosol optical depth (AOD, $\times 10^{-2}$) at 550nm in AER with respect to CTL. Only changes statistically significant at the 95% confidence level are plotted in (c) based on a Student's *t* test.

Accepted for publication in *Journal of Climate*. DOI10.1175/JCLI-D-19-0195.1.

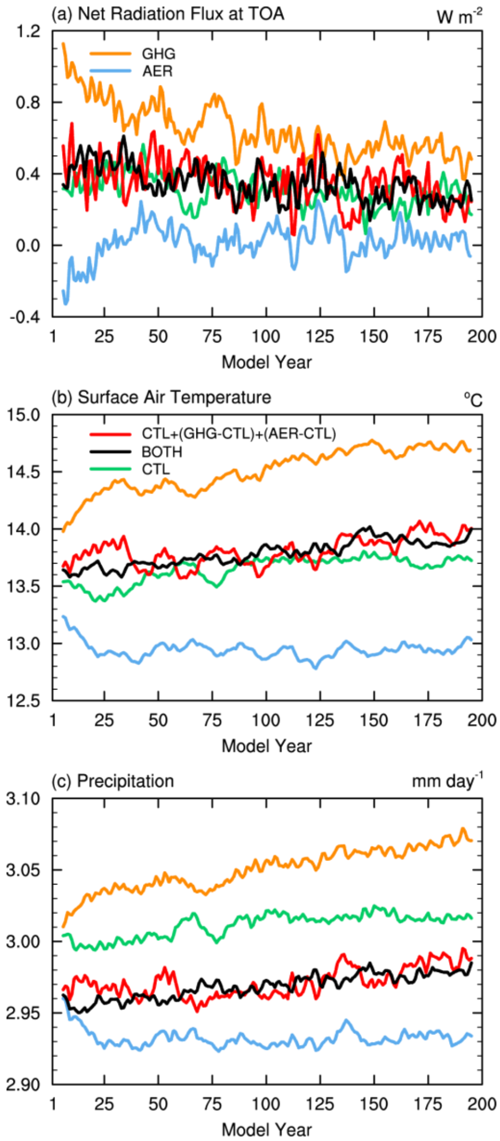

Figure 2. Time series of 11-year smoothed global-mean annual (a) net radiation flux at the top of the atmosphere (TOA, positive downward, $W{\cdot}m^{-2}$), (b) surface air temperature (Tas, ℃), and (c) precipitation ($mm{\cdot}day^{-1}$) from each of the experiments and the linear combination of CTL and changes from the GHG and AER experiments [i.e., CTL+ (GHG – CTL) + (AER – CTL), red line].

Accepted for publication in *Journal of Climate*. DOI10.1175/JCLI-D-19-0195.1.

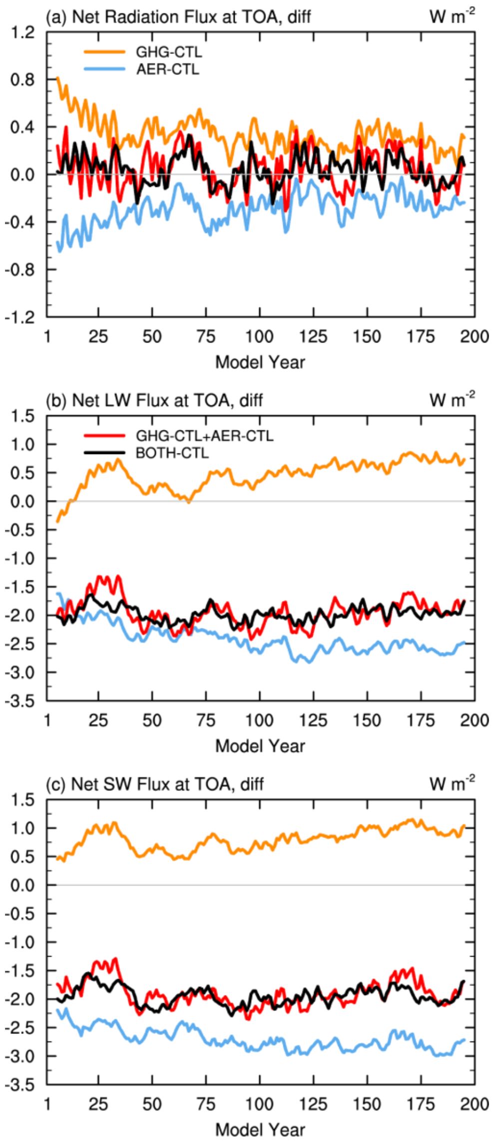

Figure 3. Time series of 11-year smoothed global-mean annual changes (relative to CTL) of (a) net radiation flux at TOA (positive downward, W·m^{-2}), (b) net longwave (LW) flux at TOA (positive upward, W·m^{-2}), and (c) net shortwave (SW) flux at TOA (positive downward, W·m^{-2}) due to the CO_2 forcing (GHG – CTL, orange line), aerosol forcing (AER – CTL, blue line), their linear combination (GHG – CTL + AER – CTL, red line), and the combined forcing (BOTH – CTL, black line).

Accepted for publication in *Journal of Climate*. DOI10.1175/JCLI-D-19-0195.1.

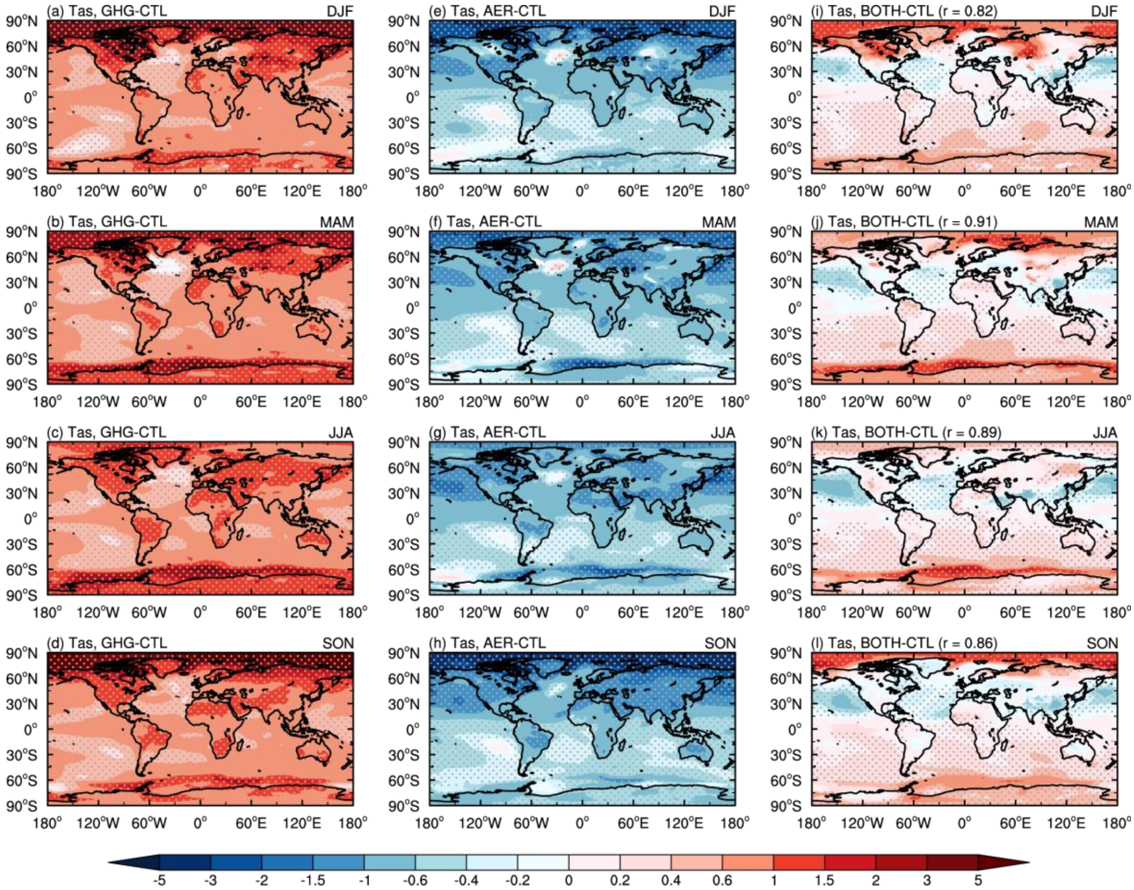

Figure 4. Seasonal-mean changes of surface air temperature (Tas, ℃) due to the (a-d) CO_2 forcing (GHG – CTL), (e-h) aerosol forcing (AER – CTL), and (i-l) the combined forcing (BOTH – CTL) for the four seasons: (a, e, i) DJF, (b, f, j) MAM, (c, g, k) JJA, and (d, h, l) SON. The stippling indicates the changes are statistically significant at the 95% confidence level based on a Student's *t* test. The spatial correlation coefficients between the linear combination of Tas responses to the individual forcings and the Tas response to the combined forcing for the four seasons are given at the top center of (i-l), respectively.

Accepted for publication in *Journal of Climate*. DOI10.1175/JCLI-D-19-0195.1.

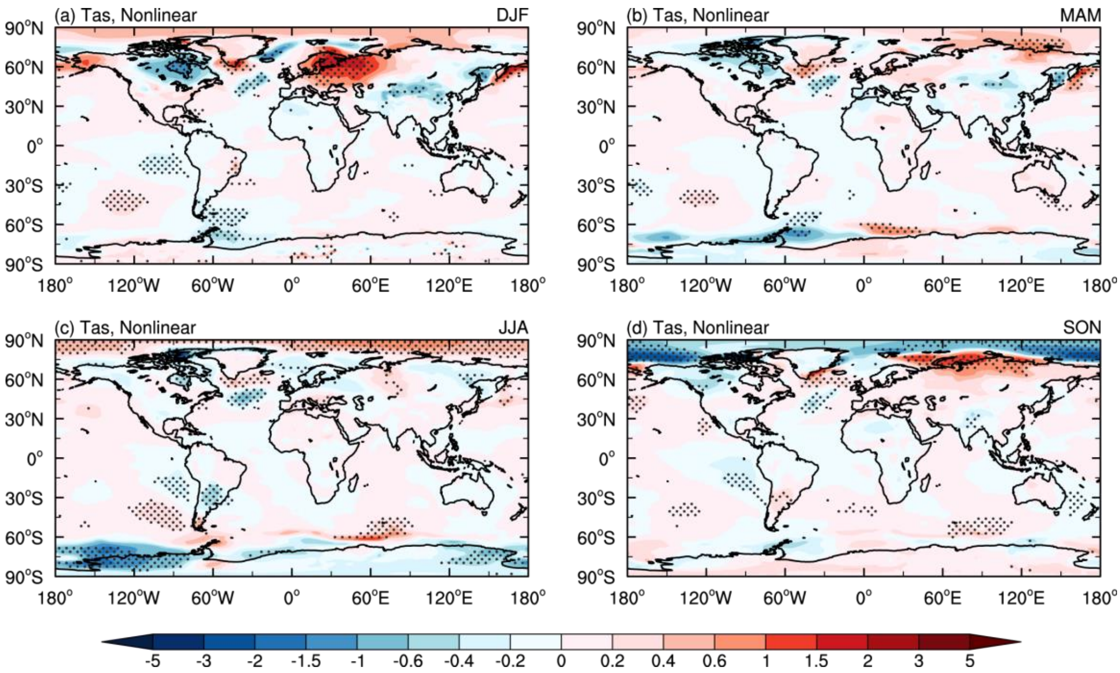

Figure 5. Seasonal-mean changes of Tas (℃) due to the nonlinear effect [i.e., (BOTH – CTL) – (GHG – CTL + AER – CTL)]: (a) DJF, (b) MAM, (c) JJA and (d) SON. The stippling indicates the changes are statistically significant at the 95% confidence level based on a Student's *t* test.

Accepted for publication in *Journal of Climate*. DOI10.1175/JCLI-D-19-0195.1.

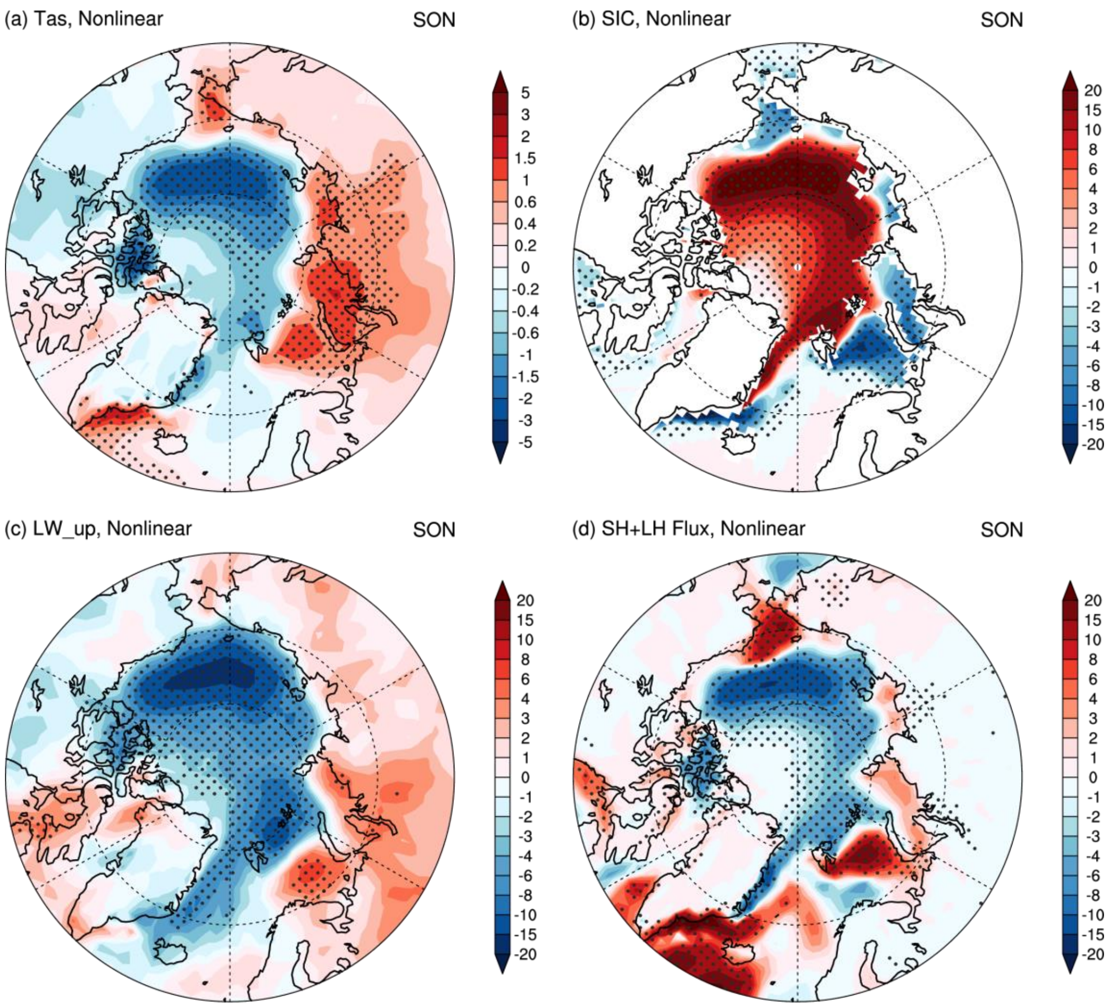

Figure 6. SON-mean changes of (a) Tas (℃), (b) sea ice concentration (SIC, % of area), (c) surface upward longwave (LW_up, W·m^{-2}), and (d) turbulent (sensible + latent) heat flux (positive upward, W·m^{-2}) due to the nonlinear effect. The stippling indicates the changes are statistically significant at the 95% confidence level based on a Student's *t* test.

Accepted for publication in *Journal of Climate*. DOI10.1175/JCLI-D-19-0195.1.

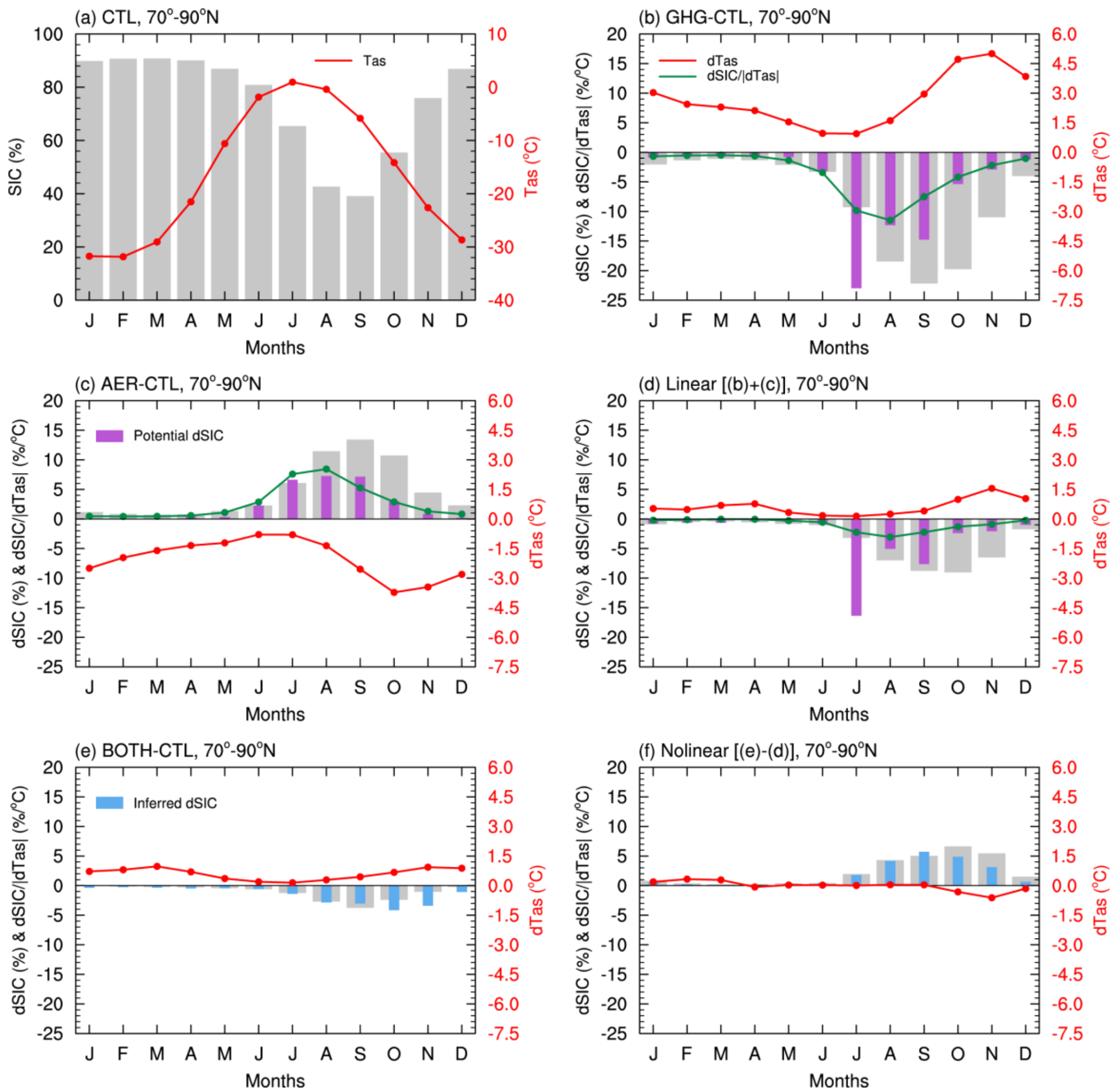

Figure 7. 150-yr mean annual cycle of SIC (grey bars, left y-axis, %) and Tas (red curves, right y-axis, ℃) averaged over the Arctic (70°–90°N) from (a) CTL and their changes due to the (b) CO_2 forcing (GHG – CTL), (c) aerosol forcing (AER – CTL), (d) their linear combination (i.e., b + c), (e) the combined forcing (BOTH – CTL), and (f) the nonlinear effect (i.e., e – d). The green curves in (b-d) indicate the SIC response to 1℃ warming or cooling, and the purple bars indicate the *potential* SIC responses diagnosed using Tas in CTL (see eqs. 6-7 in section 2c). The blue bars in (e, f) indicate the *inferred* SIC responses to the combined and nonlinear effects based on eqs. 4-5 in section 2c, respectively.

Accepted for publication in *Journal of Climate*. DOI10.1175/JCLI-D-19-0195.1.

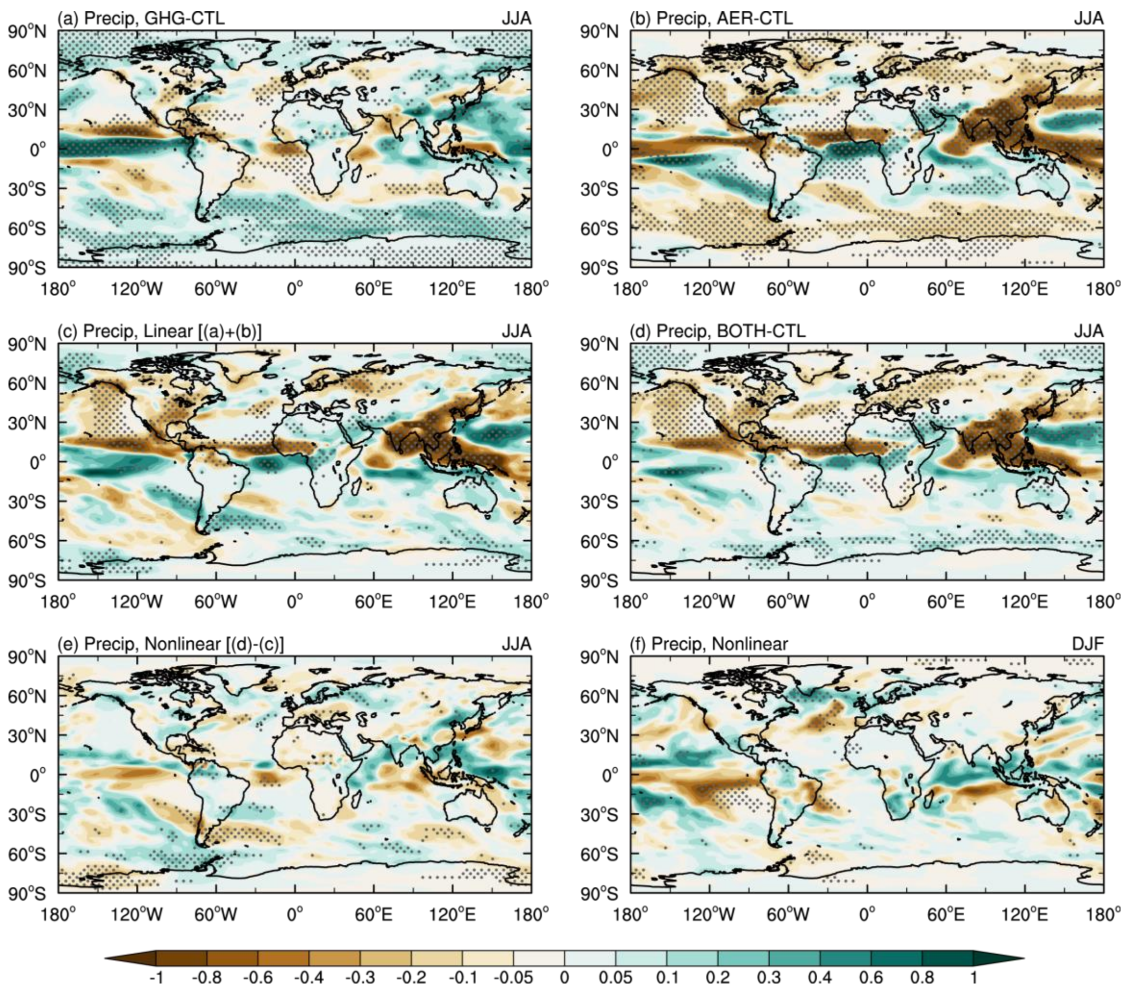

Figure 8. JJA-mean changes of precipitation (mm·day^{-1}) due to the (a) CO_2 forcing (GHG – CTL), (b) aerosol forcing (AER – CTL), (c) their linear combination (i.e., a + b), (d) combined forcing (BOTH – CTL), and (e) the nonlinear effect (i.e., d – c). (f) Same as (e) except for DJF. The stippling indicates the changes are statistically significant at the 95% confidence level based on a Student's *t* test.

Accepted for publication in *Journal of Climate*. DOI10.1175/JCLI-D-19-0195.1.

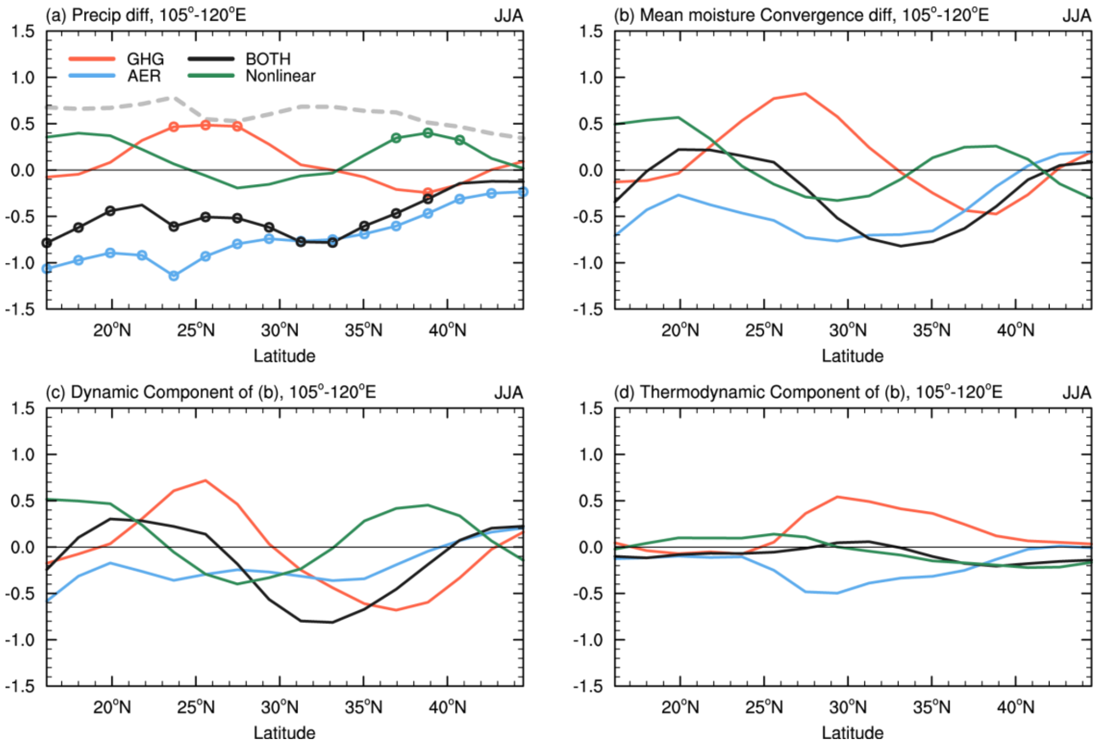

Figure 9. JJA-mean changes of (a) precipitation (mm·day^{-1}), (b) mean moisture convergence (mm·day^{-1}), and its (c) dynamic component (mm·day^{-1}) and (d) thermodynamic component (mm·day^{-1}) zonally averaged over East Asia (105°–120°E). The gray dashed line in (a) denotes the JJA-mean precipitation in CTL, which is scaled by 1/10 in order to use the same y-axis. Circles in (a) indicate the changes are statistically significant at the 95% confidence level based on a Student's *t* test.

Accepted for publication in *Journal of Climate*. DOI10.1175/JCLI-D-19-0195.1.

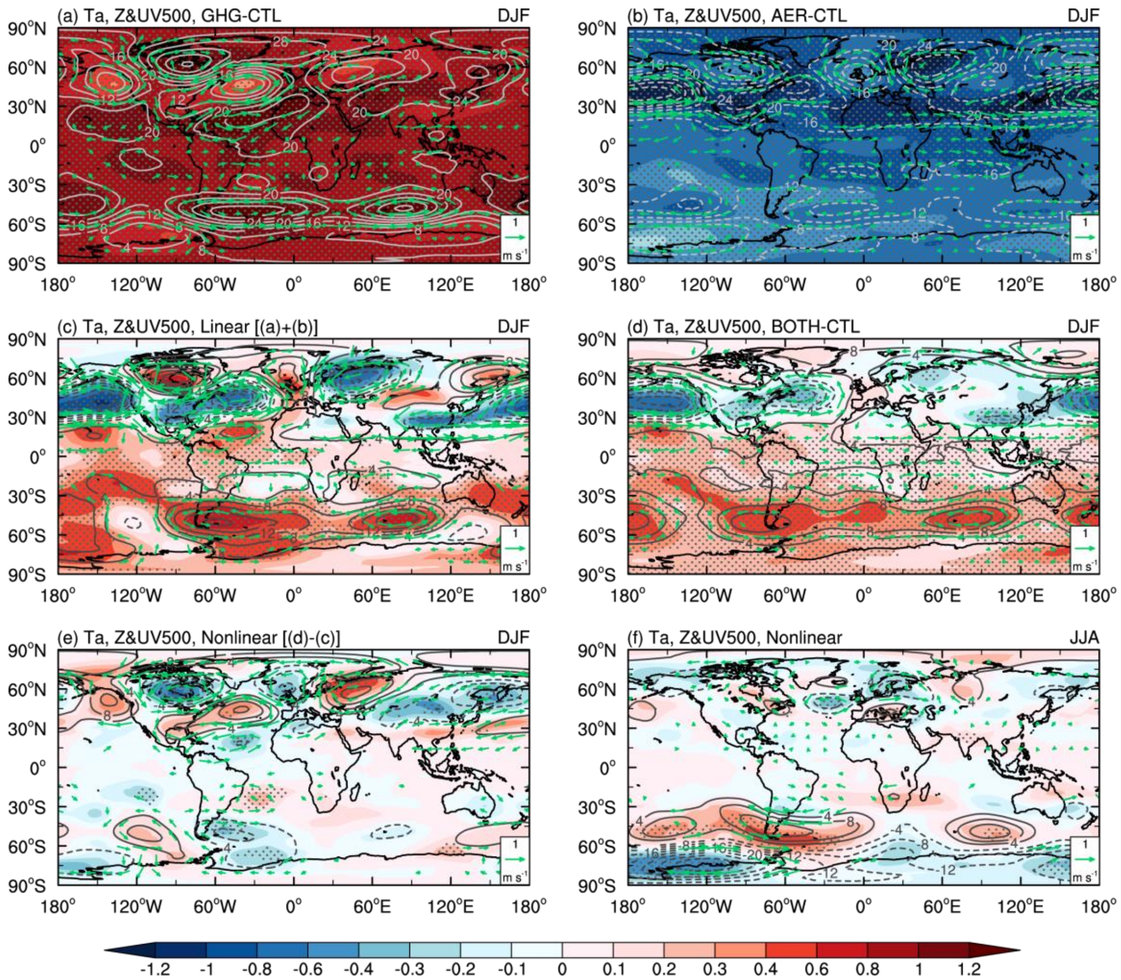

Figure 10. DJF-mean changes of 500-hPa air temperature (shading; ℃), geopotential height (contours; gpm), and horizontal winds (vectors; m·s^{-1}) due to the (a) CO_2 forcing (GHG – CTL), (b) aerosol forcing (AER – CTL), (c) their linear combination (i.e., a + b), (d) the combined forcing (BOTH – CTL), and (e) the nonlinear effect (i.e., d – c). (f) Same as (e) except for JJA. The contour interval is 4 gpm, and the zero contour is omitted for clarity. Both stippling and vectors indicate the changes are statistically significant at the 95% confidence level based on a Student's *t* test.

Accepted for publication in *Journal of Climate*. DOI10.1175/JCLI-D-19-0195.1.

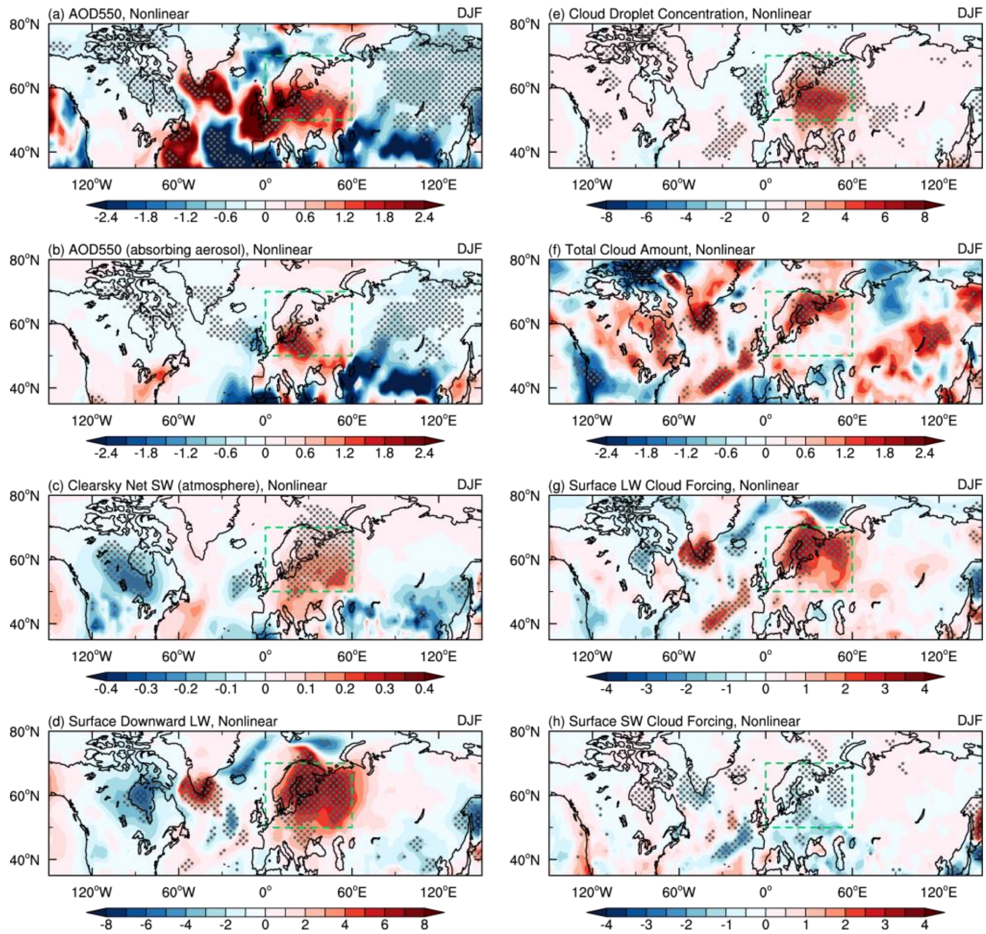

Figure 11. DJF-mean nonlinear changes of (a) aerosol optical depth (AOD) at 550nm ($\times10^{-3}$), (b) AOD at 550nm for absorbing aerosols ($\times10^{-4}$), (c) clear-sky net shortwave radiation absorbed by the atmosphere ($W{\cdot}m^{-2}$), (d) surface downward LW ($W{\cdot}m^{-2}$), (e) cloud droplet concentration ($\times10^{9}{\cdot}m^{-2}$), (f) total cloud amount (% of area), (g) LW and (h) SW surface cloud forcing ($W{\cdot}m^{-2}$, positive downward). The LW (SW) surface cloud forcing is defined as the difference between the all-sky and clear-sky net surface LW (SW) radiation (Ramanathan et al. 1989). A positive (negative) surface cloud forcing indicates that clouds enhance (reduce) the downward LW or SW at the surface, leading to a surface warming (cooling) effect. The stippling indicates the changes are statistically significant at the 95% confidence level based on a Student's *t* test. The green rectangle indicates central-northern Europe (0°–60°E, 50°–70°N).

Accepted for publication in *Journal of Climate*. DOI10.1175/JCLI-D-19-0195.1.

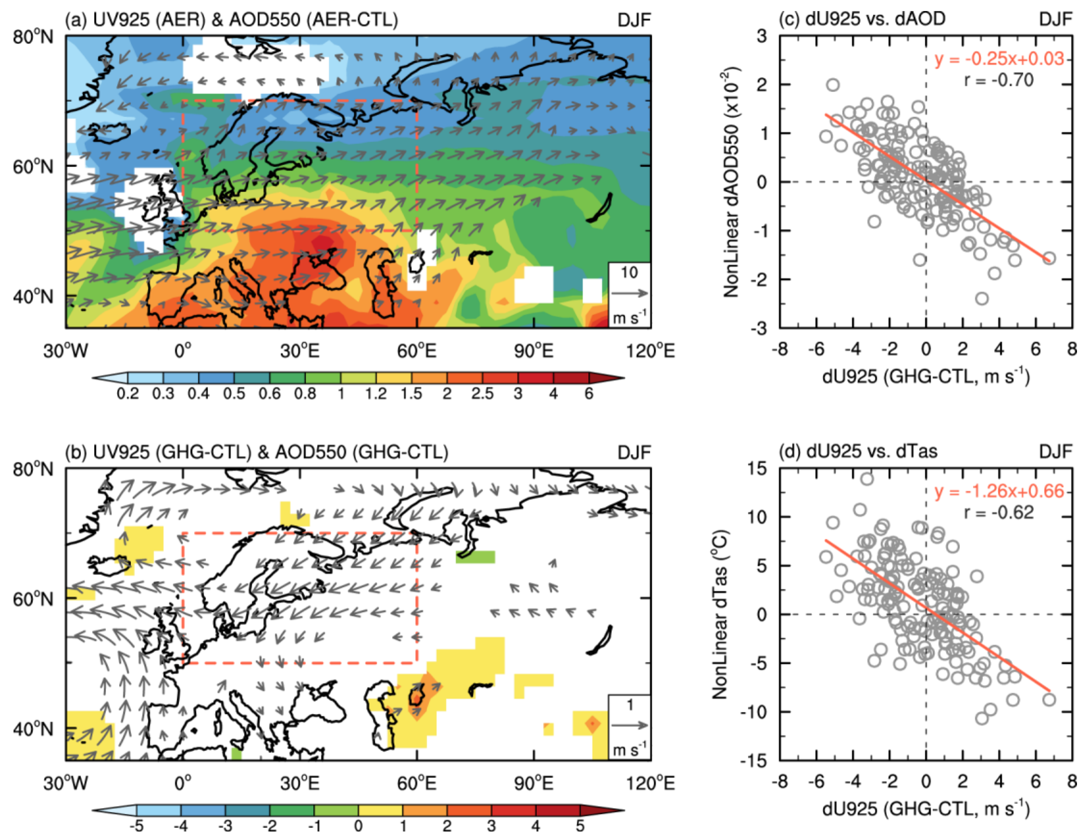

Figure 12. Spatial distributions of DJF-mean (a) AOD changes (shading, $\times10^{-2}$) in AER relative to CTL, and climatological mean 925-hPa horizontal winds in AER (vectors, $m \cdot s^{-1}$) and (b) AOD changes (shading, $\times10^{-2}$) and 925-hPa horizontal wind anomalies (vectors, $m \cdot s^{-1}$) in GHG relative to CTL. Only changes statistically significant at the 95% confidence level are plotted in (a-b) based on a Student's *t* test. The red rectangle indicates central-northern Europe (0°–60°E, 50°–70°N). (c) Scatter plot of 925-hPa zonal wind change due to the CO_2 forcing (x-axis, $m \cdot s^{-1}$) and nonlinear AOD at 550nm change (y-axis, $\times10^{-2}$) in DJF averaged over central-northern Europe. (d) Same as (c), except for 925-hPa zonal wind change due to the CO_2 forcing (x-axis, $m \cdot s^{-1}$) and nonlinear Tas change (y-axis, ℃). In (c-d), each circle indicates a model year, the red line indicates the regression line, and the regression equation and the correlation coefficient are given at the top right corner.

Accepted for publication in *Journal of Climate*. DOI10.1175/JCLI-D-19-0195.1.